Searching for Stochastic Gravitational Waves Using Co-located Interferometric Detectors

by

Nickolas Fotopoulos

B.S. in Physics, Carnegie-Mellon University

Submitted to the Department of Physics
in partial fulfillment of the requirements for the degree of

Master of Science in Physics

at the

MASSACHUSETTS INSTITUTE OF TECHNOLOGY

September 2006

Author .....
Department of Physics
September 20, 2006

Certified by .....
Erotokritos Katsavounidis
Associate Professor
Thesis Supervisor

Certified by .....
Nergis Mavalvala
Assistant Professor
Thesis Reader

Accepted by .....
Thomas J. Greytak
Associate Department Head for Education

Searching for Stochastic Gravitational Waves Using Co-located Interferometric Detectors

by

Nickolas Fotopoulos

Submitted to the Department of Physics
on September 20, 2006, in partial fulfillment of the
requirements for the degree of
Master of Science in Physics

Abstract

Despite their intrinsic advantages due to co-location, the two LIGO (Laser Interferometer Gravitational Wave Observatory) Hanford interferometers have not been used in the search for the stochastic gravitational wave background due to their coupling to a shared environment, which may be comparable to or exceed any gravitational signal. In this thesis, using data from LIGO's fourth science run, we demonstrate a technique to relate the H1-H2 coherence to coupling with physical environmental channels. We show that the correspondence is tight enough to correctly identify regions of high and low coupling and the nature of the coupling in the data set. A simple thresholding provides frequency vetoes, which we can use to derive a significantly cleaner coherence spectrum. Next, using this frequency veto technique and data from the first epoch of LIGO's fifth, currently running science run, we design, implement, and perform a search for astrophysical populations of gravitational wave emitters, which emit predominantly in the kilohertz region of the spectrum, a region totally inaccessible to detectors separated by thousands of kilometers. As well as providing us with a proof-of-concept, the results provide an advanced look at the physical results to come from H1-H2 by the end of S5.

Thesis Supervisor: Erotokritos Katsavounidis
Title: Associate Professor

Thesis Reader: Nergis Mavalvala
Title: Assistant Professor

Acknowledgments

Erik, you trusted in me when I needed it most. For that above all, I thank you. Beyond that, as my adviser, your advice has been consistently excellent. You have shown me how to ask the right questions, as well as how best to answer them.

To all of my colleagues in LIGO, and particularly, the stochastic group, thank you for taking me under your wing and showing me how it's done. You've made me feel at home. You've inspired me. Now you're stuck with me.

Stefan, what little I know about the interferometers, I learned from you. Believe it or not, you're a role model to me in a lot of ways.

Nirav, I beat you to leaving MIT, even if it wasn't quite how we thought it would be. Thank you for always, always being there for me. Even when it was my fault.

Mom, Bub, you've always given me your unconditional love and support. You not only brought me into this world, but provided me with the tools and attitude I need to achieve my dreams, no matter the dreams. Your words and deeds of encouragement carry me forward every day.

Contents

1 Introduction **15**

1.1 Gravitational Wave Phenomenology 15

1.2 LIGO Interferometers 17

1.2.1 Primary Noise Sources 19

1.2.2 LIGO Calibration 21

1.2.3 The Hanford LIGO Interferometers and the Stochastic Search 22

1.3 Stochastic Gravitational Waves 22

1.3.1 Astrophysical Gravitational Wave Background 23

1.3.2 Spectrum 24

1.3.3 Statistical Assumptions 24

1.3.4 Upper Limits 25

1.4 The Stochastic Search 26

1.4.1 The Basics, Optimal Filtering 27

1.4.2 Non-trivial geometry 29

2 Identifying Environmental Correlation in H1-H2 **31**

2.1 Introduction 31

2.2 Coherence 32

2.3 Environmental contributions to coherence 33

2.4 Implementation 38

2.4.1 Degrees of Freedom 38

2.4.2 Threshold 40

2.4.3 Caveats 41

2.5 Results 41

3 Modeling Astrophysical Gravitational Wave Spectra 47

3.1 General Technique 47

3.1.1 Source Fluence 48

3.1.2 Event Rate Density 49

3.1.3 Summary 50

3.2 Search Models 51

3.2.1 Pulsars 51

3.2.2 Magnetars 52

3.2.3 Black Hole Ringdowns 53

3.2.4 Double Neutron Star Coalescences 55

3.2.5 Neutron Star Bar Modes 57

4 A Search for Astrophysical Gravitational Radiation 59

4.1 Search Pipeline 59

4.2 Low-Frequency Validation with Hardware Injections 60

4.2.1 S4 Hardware Injections 61

4.2.2 S5a Hardware Injections 61

5 S5a H1-H2 Results 65

5.1 Data Selection 65

5.2 S5a H1-H2 Coherence Spectrum 66

5.3 Flat Ω_{gw} Spectrum 66

5.3.1 Result 66

5.3.2 Diagnostic Checks 69

5.4 Pulsar/Magnetar Results 72

5.5 Black Hole Ringdown Results 73

5.6 Double Neutron Star Coalescence Results 73

5.7 Future Prospects 74

A Analysis parameters 77

List of Figures

1-1 The effects of gravitational waves incident on a circle of point particles. The waves are linearly polarized plane waves traveling into the page. The top row indicates the + polarization state and the bottom row indicates the × polarization state. Time (and the waves' phases) increases from left to right. The strain shown here (amplitude of stretch and squeeze) is $h = 0.3$, which is at least 20 orders of magnitude larger than the gravitational wave strain we expect to observe with LIGO. . 17

1-2 This is the basic optical layout of the LIGO interferometers. From the input laser, the beam passes through the Recycling Mirror (labeled RM), then the Beam Splitter (BS), where the beam splits to enter the resonant arm cavities (X and Y arms). The resonant arm cavities are capped by the Input Test Masses (ITMs) and the End Test Masses (ETMs). 18

1-3 This is the building layout of Hanford.[1] The LVEA houses most of the optics and electronics. The H1 ETMs are in the end stations, and the H2 ETMs are in the mid stations. The Livingston site is similar, but there are no mid stations, as there is no 2km interferometer there. 19

1-4 Best LIGO sensitivity curve as of June 4, 2006 with historical comparisons[2]. $h[f]$ is defined such that the signal energy in a given frequency band is $\int h^2[f]\mathrm{d}f$. 20

1-5 The gravitational wave "landscape". It represents observational limits on gravitational waves at different frequencies as well as a few theoretical predictions for where we might expect to find gravitational waves. The LIGO S5 entries are based on projections of design sensitivity curves integrated for a full year. The H1-H2 projection further assumes no instrumental correlation. 26

1-6 H1-L1 and H1-H2 overlap reduction functions. Above 300Hz, the H1-L1 overlap reduction function is essentially zero while the H1-H2 overlap reduction function remains at one. 30

2-1 Reference coherence between H1 and H2 gravitational wave channels integrated over S4, $\Delta f = 1/32$Hz, $N_{\text{ref}} = 3.7 \times 10^4$. Note the high coherence features, both narrow and broad. The horizontal line represents $1/N_{\text{ref}} = 2.7 \times 10^{-5}$, the statistical noise floor. 34

2-2 Histograms of bin-by-bin coherence values averaged over all of S4. The thick, solid line represents the expected distribution of Γ values if the two data streams were uncorrelated. The remaining lines show histograms of coherence from real data, with the veto threshold indicated by the legend. In all cases, the 0.1Hz band surrounding injected pulsars and the 5Hz band surrounding each 60Hz harmonic were vetoed. . . . 35

2-3 Flowchart of our H1-H2 frequency veto generator. Data flows from left to right. `Hn:LSC-DARM_ERR` are the gravitational wave channels and `H0:PEM-XXXX_MIC` are examples of microphone channels. $\Gamma(f)$ denotes taking the coherence between the two input channels, `x` denotes bin-by-bin multiplication, and max denotes taking the maximum across PEM channels. 39

2-4 H1-H2 coherence with coherence product max. The upper, black dots are H1-H2 coherence with 1/32Hz frequency resolution and the horizontal line is $1/N_{\text{ref}} \approx 2.7 \times 10^{-5}$. The lower, gray dots are the IFO-PEM coherence product maxima with 1/100Hz frequency resolution and $1/N^2 \approx 10^{-8}$. 43

2-5 H1-H2 coherence with frequency vetoes, threshold=6.8×10^{-6}. The broken series of points is H1-H2 coherence with 1/32Hz frequency resolution and $1/N_{\text{ref}} \approx 2.7 \times 10^{-5}$. Only frequency bins surviving the veto threshold of 6.8×10^{-6} are displayed. Additionally, the 0.1Hz band surrounding injected pulsars and the 5Hz band surrounding each 60Hz harmonic were vetoed. 44

2-6 H1-H2 coherence with frequency vetoes, threshold=3×10^{-7}. The broken series of points is H1-H2 coherence with 1/32Hz frequency resolution and $1/N_{\text{ref}} \approx 2.7 \times 10^{-5}$. Only frequency bins surviving the veto threshold of 3×10^{-7} are displayed. Additionally, the 0.1Hz band surrounding injected pulsars and the 5Hz band surrounding each 60Hz harmonic were vetoed. 45

3-1 Expected stochastic gravitational wave background due to pulsars spinning down throughout the universe. Magnetar spindowns will have the same spectral shape, but an amplitude 10× greater. 53

3-2 Expected stochastic gravitational wave background due to black holes forming and ringing down throughout the universe. 55

3-3 Expected stochastic gravitational wave background due to double neutron star mergers throughout the universe. 58

4-1 Flowchart of the pipeline used in this thesis to measure stochastic backgrounds of astrophysical gravitational waves. The LIGO stochastic analysis is described in references [9], [10], and [12]. 60

5-1 S5a H1-H2 coherence and the IFO-PEM coherence product maxima approximation. The top trace is the direct H1-H2 coherence and the lower trace represents the coherence product maxima. The gray, horizontal line at $1/N \approx 10^{-5}$ is the noise floor of the former. 67

5-2 Normalized coherence histograms for surviving S5a H1-H2 coherence after veto. 68

5-3 The running point estimate of the S5a H1-H2 flat Ω_{gw} stochastic analysis. At each time, the ordinate is the point estimate as integrated over all prior data. The blue region is the 90% confidence region, i.e., 1.65σ. The data shown have been smoothed via interpolation. 70

5-4 S5a H1-H2 coherence and the IFO-PEM coherence product maxima approximation, with threshold= 4.02×10^{-8} vetoed regions highlighted in red. The top trace is the direct H1-H2 coherence and the lower trace represents the coherence product maxima. The gray, horizontal line at $1/N \approx 10^{-5}$ is the noise floor of the former. 71

5-5 Top: H1 and H2 interferometer strain noise curves as measured in January 2006, about midway through S5a. Middle: H1-H2 stochastic search sensitivity integrand, with vetoes applied. Frequencies with larger sensitivity integrands contribute more to the point estimate. Units are not particularly meaningful, so we omit them. The scaling on the y axis is logarithmic. Integrating from low frequency to high, 1% and 99% accumulated sensitivity percentiles are 77.25Hz and 160.84375Hz, respectively. Bottom: Coherence from frequency bins which survive the frequency veto with threshold 4.02×10^{-8}. The grey, dashed line indicates $1/N$, the coherence noise floor, and the red, dashed line indicates $10.4/N$, the coherence level below which one would expect all coherences, were the coherence all drawn from an uncorrelated distribution ($\exp(-N\Gamma)$), with a false rate of approximately 1 in 32768. 72

List of Tables

1.1 LIGO S1 Results by interferometer pair. σ is the standard deviation of our measurement on Ω_{eff}. We assume a reduced Hubble constant of $h_{100} = 0.72$. [10] 23

4.1 S4 hardware injection results for H1-L1 and H2-L1 pairs. All injections were successfully recovered for both pairs. Start time is in GPS seconds and duration is in seconds. 61

4.2 S4 hardware injection results for H1-H2. Thresholds are applied to the coherence product maxima to produce frequency vetoes, as described in chapter 2. Start time is in GPS seconds and duration is in seconds. 62

4.3 S5a hardware injection results for H1-L1 and H2-L1 pairs during triple coincidence times only. Both injections were successfully recovered for both pairs. Start time is in GPS seconds and duration is in seconds. . 62

4.4 S5a hardware injection results for H1-H2 pairs during triple coincidence times. Thresholds are applied to the coherence product maxima to produce frequency vetoes, as described in chapter 2. We expect and assume an 11% systematic uncertainty, based on S4 calibrations. Start time is in GPS seconds and duration is in seconds. 63

5.1 S5a H1-H2 Flat Spectrum Results. Error bars represent statistical uncertainty, then calibration uncertainty. SNR is calculated using the root sum squares of the uncertainties. The final two columns hold the fraction of bandwidth remaining after veto. In-band BW refers to the entire analysis band of 40-500Hz. Sensitive BW refers to the frequency region between the 1st and 99th percentiles of cumulative sensitivity (as integrated over frequency), or 77.25-160.84375Hz. Calibration uncertainty is assumed to be 11%. 69
5.2 S5a H1-H2 Pulsar/Magnetar Results 73
5.3 S5a H1-H2 Blackhole Ringdown Results 73
5.4 S5a H1-H2 Double Neutron Star Coalescence Results 74

A.1 Analysis parameters used in the stochastic searches of this thesis. . . 78
A.2 PEM channels used to generate vetoes, original sampled rates, and the downsampled rate used. 79
A.3 PEM channels used to generate vetoes, original sampled rates, and the downsampled rate used (continued). 80
A.4 PEM channels used to generate vetoes, original sampled rates, and the downsampled rate used (continued). 81

Chapter 1

Introduction

This introductory chapter will give an overview of the LIGO instrumentation, define the gravitational signals of interest, and review the basics of detection. Chapter 2 examines how correlations specifically of environmental origin can be identified and excised, leaving behind a significantly better behaved data set, perhaps allowing us to execute a stochastic search with co-located detectors for the first time. Chapter 3 steps through the physical models of several gravitational wave emitters, developing theoretical spectra for which we can search. Chapter 4 discusses the final pipeline which combines the developments of chapters 2 and 3 and reviews pipeline validation through hardware injections. Chapter 5 contains the final results of this thesis work and directions for future research.

1.1 Gravitational Wave Phenomenology

In a famous two sentence summary of Einstein's general relativity (GR), the great relativist John Archibald Wheeler stated[8],

> Matter tells space how to curve.
> Space tells matter how to move.

More verbosely, GR provides dynamics for spacetime's curvature based on its mass and energy contents, as well as dynamics describing what trajectories particles will

take when passing through curved spacetime. Curvature itself carries energy, and gravitational waves are self-propagating waves of this spacetime curvature. Gravitational waves arise very naturally in considering metric perturbations to otherwise flat spacetime. We will discuss their production later, but for now will focus on salient predicted features and the resulting effects whereby they are detectable.

Gravitational waves, like electromagnetic waves, are transverse waves, propagate with the speed of light, have two independent polarizations, and follow a $1/r^2$ falloff in *energy*, which corresponds to a $1/r$ falloff in electric field strength and gravitational wave strain. Gravitational wave detectors like LIGO are often referred to as gravitational antennas or gravitational telescopes, in analogy to radio wave detectors which are radio antennas and in astronomers' hands become radio telescopes.

The polarization states of gravitational waves are rather different from the polarizations of light. For linearly polarized light normally incident on a polarization-sensitive detector, one would have to rotate the detector π radians about the beam axis in order to go from maximum signal to minimum signal and back to maximum signal. For a gravitational wave in an identical setup, one would only have to rotate the detector $\pi/2$ radians to go through the same cycle. These symmetries are consistent with "plus" $(+)$ and "cross" $(\times)$ polarization states, $\pi/4$ radians apart, versus horizontal and vertical polarization states for light, $\pi/2$ radians apart. This is consistent with gravitational fields being spin-2 and electromagnetic fields being spin-1.

The effect of monochromatic, linearly polarized gravitational incident on a small patch of spacetime is to sinusoidally squeeze and stretch it and its contents along one axis, then along the perpendicular, all in the plane transverse to the direction of propagation. The process is best described by the diagram of figure 1-1. The amplitude of fractional length change $(\delta L/L)$ along an optimally oriented axis is half the gravitational wave strain. The instantaneous *difference* in fractional lengths between perpendicular arms (differential strain, $\delta L_1/L_1 - \delta L_2/L_2$) has amplitude equal to the gravitational wave strain. The strain of gravitational waves incident onto the Earth are expected to be of order 10^{-21} or smaller. For two perpendicular

rods, each of length 4km, this corresponds to a differential displacement $(\delta L_1 - \delta L_2)$ of 4×10^{-18}m, which is three orders of magnitude smaller than the radius of an atomic nucleus.

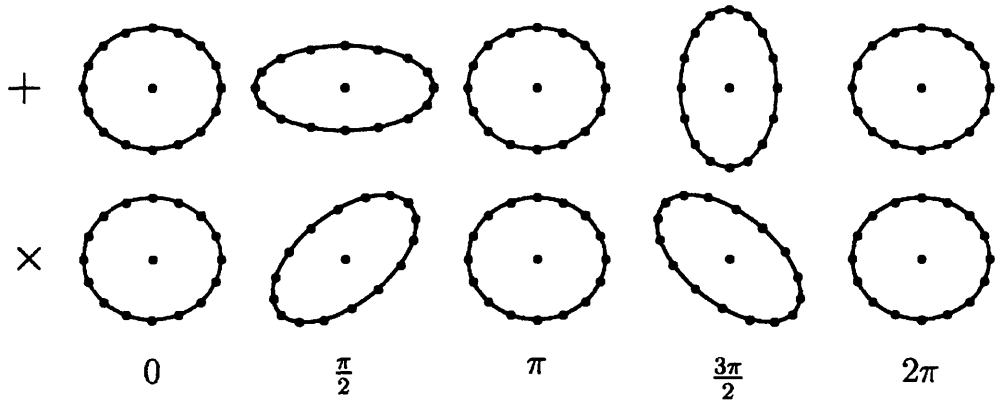

Figure 1-1: The effects of gravitational waves incident on a circle of point particles. The waves are linearly polarized plane waves traveling into the page. The top row indicates the + polarization state and the bottom row indicates the × polarization state. Time (and the waves' phases) increases from left to right. The strain shown here (amplitude of stretch and squeeze) is $h = 0.3$, which is at least 20 orders of magnitude larger than the gravitational wave strain we expect to observe with LIGO.

1.2 LIGO Interferometers

The Michelson interferometer is an ideal apparatus for gravitational wave detection. It has exquisite sensitivity for differential length changes in its arms. In broad outline, the LIGO detectors are power-recycled Michelson interferometers with resonant arm cavities, as we see in figure 1-2[11]. We will assume familiarity with a basic Michelson interferometer. A power-recycling mirror allows for power buildup in the interferometer. Power buildup in well-tuned resonant arm cavities magnifies strain sensitivity in the interference fringe by a few orders of magnitude. Those resonant arm cavities are capped by input test masses (ITMs) and end test masses (ETMs), which are suspended mirrors. The mirrors, as well as every other optic, are seismically isolated by complex, multiple pendulum systems such that we may approximate them as inertial bodies along the beam axis. It is the differential displacement $(\delta L_1 - \delta L_2)$

between these inertial cavities that is revealed at the readout port (also known as the anti-symmetric port or dark port) and converted to differential strain.

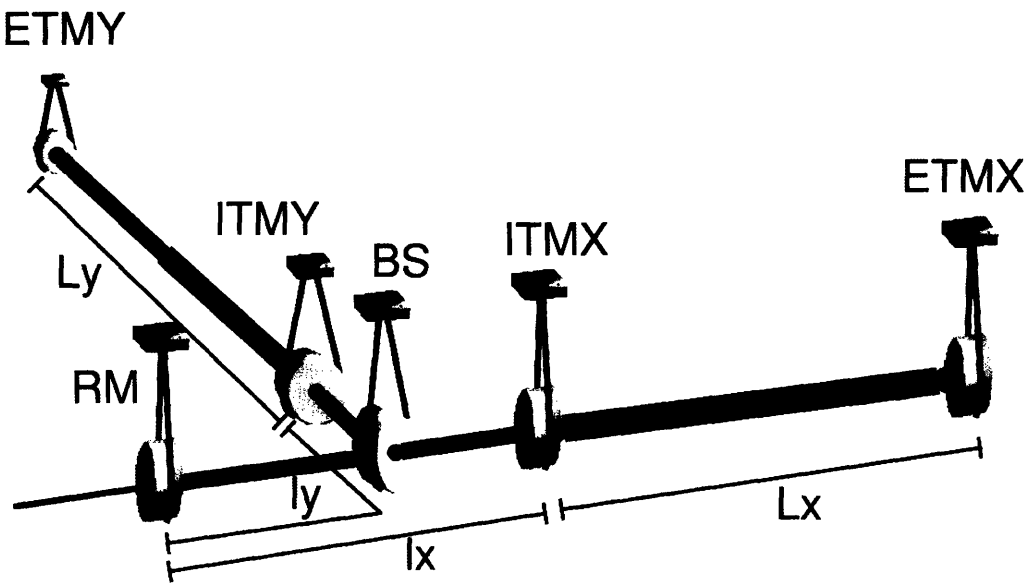

Figure 1-2: This is the basic optical layout of the LIGO interferometers. From the input laser, the beam passes through the Recycling Mirror (labeled RM), then the Beam Splitter (BS), where the beam splits to enter the resonant arm cavities (X and Y arms). The resonant arm cavities are capped by the Input Test Masses (ITMs) and the End Test Masses (ETMs).

Adding slightly more detail, the entire interferometer is enclosed within ultra high vacuum beam tubes, achieving a gas pressure of less than 10^{-9} torr, the largest vacuum system ever constructed. The input optics, beam splitter, and readout table are all in a common room called the LVEA (Laser Vacuum Equipment Area), as depicted in figure 1-3. There are three LIGO interferometers between two sites, both in the United States, separated by 3002km. In Livingston Parish in the state of Louisiana, there is a 4km interferometer named L1. At the Hanford Nuclear Reservation in the state of Washington, there are two interferometers of arm length 4km and 2km, dubbed H1 and H2, respectively. Both Hanford interferometers utilize the same evacuated beam tubes and LVEA, but separate buildings to house their respective ETMs.

LIGO has reached or exceeded design sensitivity[3] in all of its instruments and S5

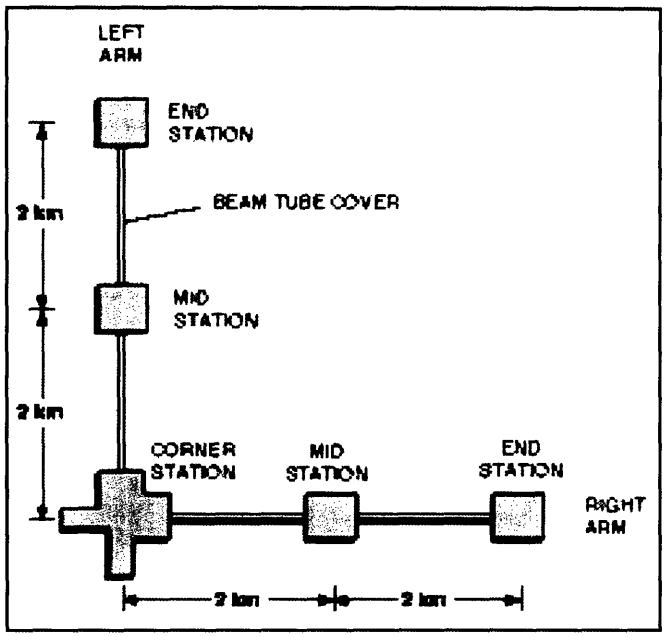

Figure 1-3: This is the building layout of Hanford.[1] The LVEA houses most of the optics and electronics. The H1 ETMs are in the end stations, and the H2 ETMs are in the mid stations. The Livingston site is similar, but there are no mid stations, as there is no 2km interferometer there.

(science run 5) has commenced. This thesis describes a technique to identify frequencies of significant instrumental correlation between the LIGO (Laser Interferometer Gravitational Wave Observatory) instruments H1 and H2, the 4km and 2km interferometers at Hanford, Washington. Removing those frequencies, we gain the use of H1 and H2 for the stochastic search, which adds a significant advantage, given their geometry, opening the window to kilohertz gravitational waves.

1.2.1 Primary Noise Sources

The LIGO interferometers are complicated instruments. The current sensitivities are the product of careful design and intensive noise hunting efforts. Figure 1-4 shows current snapshots of best achieved strain noise among all of the LIGO interferometers. The SRD (Science Requirements Document[3]) curve is a composite of three fundamental noise sources in the instrument. What proceeds is a description of those dominant noise sources limiting the current interferometer sensitivity.

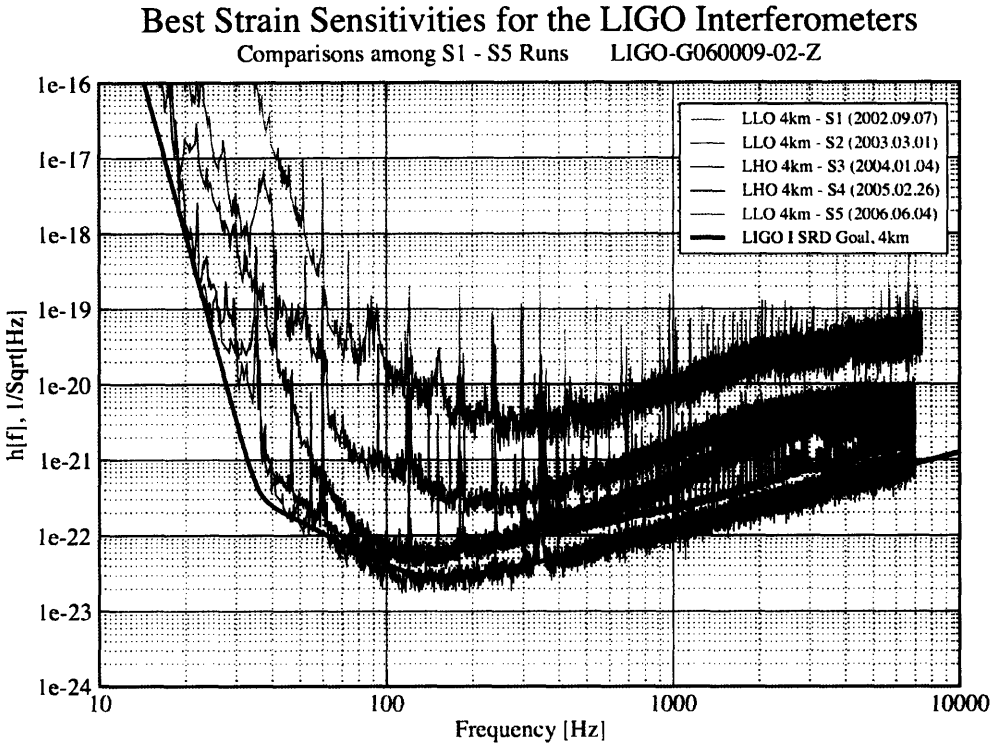

Figure 1-4: Best LIGO sensitivity curve as of June 4, 2006 with historical comparisons[2]. $h[f]$ is defined such that the signal energy in a given frequency band is $\int h^2[f]\mathrm{d}f$.

The SRD curve shows three distinct slopes (in log-log space). At low frequencies, from 0Hz to approximately 40Hz, the noise floor is seismic in origin. Multiple-pendulum systems attenuate low-frequency disturbances rapidly, $h \propto f^{-14}$ in this plot. The slope of the curve is vertical enough that it has become known as the "seismic wall". L1 has been upgraded to an active seismic isolation system called HEPI (Hydraulic External Pre-Isolation) due to excessive seismic noise in the local environment, such as construction, logging, and passing trains.

At the high-frequency end, 150Hz and beyond, we have shot noise. Shot noise arises from photon counting statistics in resolving the phase shift between the arms. The interferometer mirrors are controlled to sit at an interference null, so that any differential arm length changes appear as light. $h \propto f$, and in the present configu-

ration, the floor can be lowered by increasing laser power. However, for Advanced LIGO, photons in squeezed quantum states may be used to improve the statistics and thereby improve sensitivity[15].

In the intermediate frequency range of 40-150Hz, we observe thermal noise. Thermal fluctuations in the mirror cause spontaneous, stochastic excitations of (primarily) the fundamental pendulum mode[26][17]. While every optic has thermal fluctuations, the pendulum mode produces the greatest and only limiting noise in this band, at present. A few ways one can drive down thermal noise are by changing the suspension material or geometry to that of higher effective Q (quality factor) and lowering operating temperature to cryogenic levels[16].

While we have covered the three noise floors comprising the SRD noise curve, in practice, there are many spectral lines on top of them (refer back to figure 1-4). At every harmonic of 60Hz is the "60Hz comb", caused by the 60Hz alternating current in United States electrical power transmission system. Every harmonic of violin modes in the suspensions stands out, as well as numerous other mechanical resonances, to varying degrees. There are times when the noise floor is elevated. High winds, construction, logging, and passing trains couple to the interferometers through the buildings which house the optics. Daily traffic patterns on nearby roadways cause diurnal variation in low frequency noise.

1.2.2 LIGO Calibration

What is actually collected at the dark port is a discrete number of photodetector counts in each sample period. To convert this to strain, $h(t)$, we must use our knowledge of the instrument to apply the appropriate gains. Calibration is generally done in the frequency-domain and only converted back to time-domain if a time-series is explicitly required. The official reference calibration document for S4 is available online[14].

The net calibration uncertainty in S4 is approximately 8% for H1 and H2 and 5% for L1, and will likely be similar for S5. In the stochastic search, we use two interferometers, so the uncertainty in the result is the quadrature sum of the individual

uncertainties. H1-L1 and H2-L1 results will have 9% uncertainty and H1-H2 will have 11% uncertainty.

1.2.3 The Hanford LIGO Interferometers and the Stochastic Search

In the search for the stochastic gravitational wave background, H1-H2 as a pair is potentially more sensitive than the H1-L1 by roughly an order of magnitude for initial LIGO[1], but H1-H2 has not yet provided a trusted result for the stochastic search. The lasers, photodiodes, associated optics, and electronics for both Hanford interferometers are located outside of the vacuum envelope in a shared room. Co-location and co-alignment remove the geometric sensitivity penalty, quantified by the overlap reduction function[23], at all frequencies, but co-location unavoidably entails immersion in a common, noisy environment.

In a search for a faint, persistent correlation, this is a severe problem. Our inability to handle instrumental correlations between H1 and H2 has thus far prevented their use together in the stochastic search. Table 1.2.3 summarizes each interferometer pair's estimate of the effective stochastic background strength, Ω_{eff}, during LIGO's first science run (S1) assuming a flat Ω_{gw} (to be defined in section 1.3.2). H1-H2's point estimate is thoroughly inconsistent with zero and is negative, unequivocally indicating the presence of cross-correlated noise. This thesis describes an attempt to use data from PEMs (Physical Environmental Monitors) to remove those frequencies with instrumental correlations and potentially gain the use of the Hanford interferometer pair for the analysis of the currently running S5 data set[2] and beyond.

1.3 Stochastic Gravitational Waves

From a detection standpoint, it makes a tremendous difference if our analyses are listening for a distant collective muttering, a distinct thunderclap, the ring of a bell,

[1]The potential sensitivity advantage also exists for Advanced LIGO, but is greatly reduced due to improved sensitivity at low frequencies.

IFO pair	Ω_{eff}	σ	$\Omega_{\text{eff}}/\sigma$
H1-H2	-16	1.8	-8.8
H1-L1	62	34	1.8
H2-L1	0.31	33	$9.4 \cdot 10^{-3}$

Table 1.1: LIGO S1 Results by interferometer pair. σ is the standard deviation of our measurement on Ω_{eff}. We assume a reduced Hubble constant of $h_{100} = 0.72$. [10]

or a single, vibrato note. In the pursuit of gravitational radiation, we distinguish between target sources and design specialized search algorithms accordingly.

Continuous wave searches target sources which radiate continuously; pulsars are persistent electromagnetic emitters of radiation and are believed to be continuous sources of gravitational radiation as well. Inspiral searches look for the distinctive signature of the radiation emitted before the coalescence of two compact objects, and the subsequent ringing as asymmetry is radiated away. Burst searches target waves passing through the detector which are well localized in time, as we expect from supernovae and compact object coalescences. Finally, stochastic searches seek to characterize the ensemble of gravitational wave sources that are past our ability to detect individually. There are two distinct classes of stochastic waves: those of cosmological origin, cast off in the immediate aftermath the Big Bang, and those of astrophysical origin, which emanate from much more recent, condensed objects we know as stars, white dwarfs, neutron stars, and black holes. This thesis relates only to the stochastic background, so will not detail the other classes of gravitational radiation any further.

1.3.1 Astrophysical Gravitational Wave Background

Rifling through our catalogues of known astronomical systems, we find only a few objects with sufficient mass, sufficient asymmetry, and sufficient acceleration to throw off appreciable quantities of gravitational radiation. Rather generically, the length and time scales of neutron stars and stellar-mass black holes dictate that their radiation spectra will peak within a factor of a few around 1kHz. Supermassive black hole and white dwarf systems will radiate predominantly below 0.001Hz.

Depending on the dominant contributors, we expect varying degrees of anisotropy. Directional searches will always make it a point to look closely in the direction of the Virgo cluster, as Virgo is the nearest galaxy cluster to Earth and thus is probably home to the most detectable unresolvable populations. Recently, Stefan Ballmer developed an analysis[7] that measures the stochastic gravitational radiation from each point on the sky assuming that there is a point source at each pixel location.

1.3.2 Spectrum

Stochastic gravitational radiation is usually quantified by $\Omega_{\rm gw}(f)$, the ratio of energy contained in gravitational waves, $\rho_{\rm gw}$, in the vicinity of frequency f to the energy required to close the universe, $\rho_{\rm critical} = 3H_0^2/(8\pi G)$. Formally, it is given by the expression:

$$\Omega_{\rm gw}(f) \equiv \frac{1}{\rho_{\rm critical}} \frac{{\rm d}\rho_{\rm gw}}{{\rm d}\ln f}. \tag{1.1}$$

Its definition involves $\ln f$ so that $\Omega_{\rm gw}(f)$ is dimensionless. This form is sometimes shared by the other major cosmological background, the cosmic microwave background (CMB).

The seminal paper which describes the stochastic search as performed by the LSC (LIGO Scientific Collaboration) is by Bruce Allen and Joseph Romano[5]. Section 1.3 more or less summarizes several sections of their paper, highlighting the equations and discussions most relevant to and setting the notation for this thesis. We refer readers to the Allen and Romano paper to clear up any ambiguity in the discussion below.

1.3.3 Statistical Assumptions

In constructing the foundations of our signal processing strategy, we utilize four simplifying assumptions. We assume the background is isotropic, unpolarized, stationary, and Gaussian. For discussion of each of these assumptions, we refer once again to Allen and Romano[5]. While we expect the stochastic background to adhere to our

assumptions, we know that terrestrial detectors, firmly planted upon the heavily trafficked Earth, cannot; real detector streams will be non-stationary and non-Gaussian. The LIGO stochastic search makes stationarity cuts and tests the Gaussianity of the data.

1.3.4 Upper Limits

The only firm theoretical bound on $\Omega_{\rm gw}(f)$ in observable frequencies (of order 10-1000Hz for terrestrial detectors and $10^{-4}-10^{-1}$ for the proposed space interferometer, LISA[19]) arises from standard Big Bang nucleosynthesis (BBN) models, and it only applies to the cosmological background. A calculation of this bound with modern parameters[22] is:

$$\int \Omega_{\rm gw}(f)\,\mathrm{d}\ln f < 1.1\times 10^{-5}(N_\nu - 3). \tag{1.2}$$

Here, N_ν is the effective number of light, relativistic particles present during BBN. Measurements have provided a 95% confidence upper limit of $N_\nu - 3 < 1.3$[13].

This bound is generally considered weak since it does not constrain the shape of $\Omega_{\rm gw}(f)$ at all and *a priori*, few expect the cosmological background to be very strong anyway[20].

Experimental upper limits on the $\Omega_{\rm gw}(f)$ have come from studying the cosmic microwave background, timing millisecond pulsars, doppler-tracking man-made spacecraft, and running instruments dedicated to detecting gravitational waves, such as cryogenic bars and earlier LIGO science runs[20][10]. Some of these have beat the BBN bound, but in completely different frequency bands than LIGO. LIGO will certainly beat the BBN bound in either the current S5 science run or the next. The expected gravitational radiation from various cosmological models along with past and future upper limits are shown in the "landscape" plot of figure 1-5. Note that the very best projected upper limits involve co-located interferometers. This thesis attempts to tap into some of H1-H2's superior sensitivity.

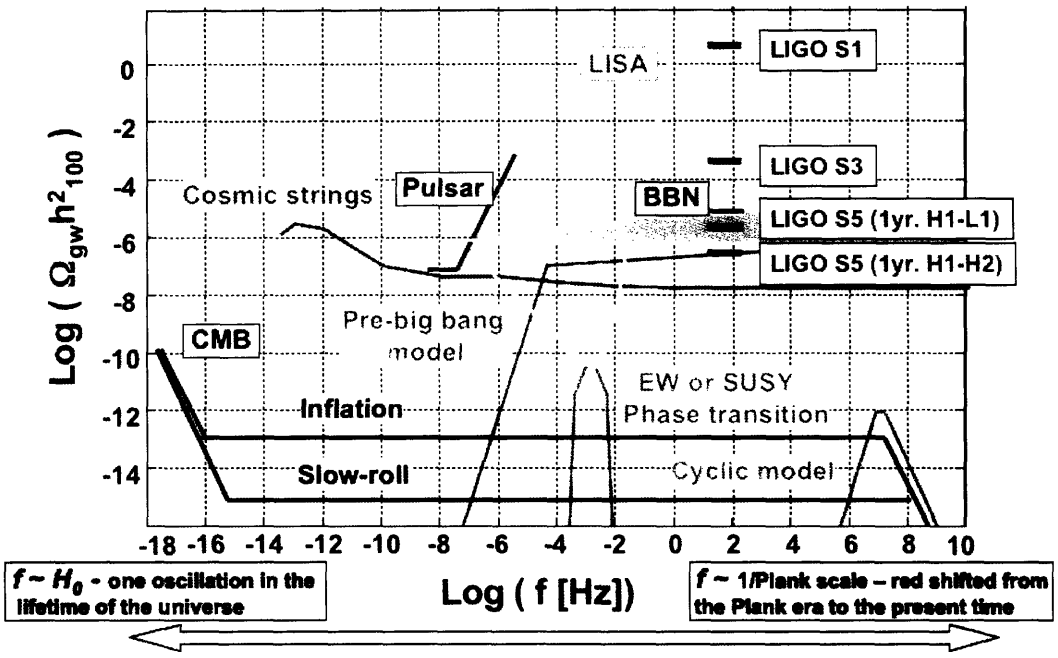

Figure 1-5: The gravitational wave "landscape". It represents observational limits on gravitational waves at different frequencies as well as a few theoretical predictions for where we might expect to find gravitational waves. The LIGO S5 entries are based on projections of design sensitivity curves integrated for a full year. The H1-H2 projection further assumes no instrumental correlation.

1.4 The Stochastic Search

While a stochastic background can be detected with a single detector (recall Penzias and Wilson discovering the CMB[4]), it requires high signal to noise and considerable confidence that one knows all of the instrument's noise sources. Cross-correlating two detector streams yields far deeper sensitivity. It has been shown that even with many interferometers at one's disposal, it is best to cross-correlate them in pairs and then combine results[5][21].

To simplify derivation, we will first consider co-located detectors and then generalize, with the overlap reduction function, to more complicated geometry. Also, as in Allen and Romano[5], we will begin by assuming that detector noise is stationary, Gaussian, independent of other detectors' noise, and much larger than the signal we seek. This section will highlight the equations and concepts most necessary to con-

duct a stochastic search. The subsequent sections will handle the more complicated situations where we relax these assumptions or deal with an important effect of dealing with real data. The case of combining multiple detector pairs is omitted, as it is beyond the scope of this work.

1.4.1 The Basics, Optimal Filtering

The inputs to the stochastic search are the differential strain channels from two gravitational wave detectors. We model these time-series as the linear sum of all the sources of noise intrinsic to the detector and a persistent gravitational wave signal. The instruments are assumed to respond identically to gravitational waves and share the same beam tubes (i.e., H1 and H2, but both the same length). The noise spectrum does not vary in shape or intensity over time. Noise in one detector is statistically independent of noise in the other.

Our signal model gives the signal, as measured by each of the detectors, s_1 and s_2, in terms of the true gravitational strain, h, and statistically independent noise in each instrument, n_1 and n_2.

$$s_1(t) = h(t) + n_1(t) \tag{1.3}$$

$$s_2(t) = h(t) + n_2(t) \tag{1.4}$$

We take the cross-correlation statistic by taking the product of the two streams and integrating over the extent of our data set, T. We use Wiener filtering to maximize our signal. Let $\tilde{\cdot}$ denote a frequency-domain function, Fourier Transformed from a time-domain function.

$$Y = \int_{-T/2}^{T/2}\int_{-T/2}^{T/2} s_1(t)Q(t-t')s_2(t')\,\mathrm{d}t \tag{1.5}$$

$$= \int_{-\infty}^{\infty}\int_{-\infty}^{\infty} \delta_T(f-f')\tilde{s}_1^*(f)\tilde{Q}(f')\tilde{s}_2(f')\,\mathrm{d}f\,\mathrm{d}f'. \tag{1.6}$$

$\delta_T(f-f')$ is a sinc function approximation to the delta function that arises from integrating over finite time. $Q(f')$ is the optimal (Wiener) filter and is given up to a normalization factor, λ, either in terms of the physical quantity we desire to know, $\Omega_{\rm gw}(f)$, or in terms of the one-sided gravitational wave strain power at the detector that we directly measure, $S_{\rm gw}(f) = 3H_0^2\Omega_{\rm gw}(f)/(10\pi^2 f^3)$. H_0 is the Hubble constant.

$$\tilde{Q}(f) = \lambda \frac{\Omega_{\rm gw}(f)}{f^3 P_1(f) P_2(f)} \tag{1.7}$$

$$= \lambda' \frac{S_{\rm gw}(f)}{P_1(f) P_2(f)} S_{\rm gw}(f) \tag{1.8}$$

$P_1(f)$ and $P_2(f)$ are one-sided strain noise power spectra of the two detectors. In either case, we need to estimate the target spectrum to conduct an optimal search. In chapter 3, we will review several models of various astrophysical $\Omega_{\rm gw}(f)$ spectra and their conversion to optimal filters. It is important to note that only the spectral shape matters, as the stochastic search will essentially return the best-fit scaling factor.

Finally, we need to characterize the mean and variance of the cross-correlation statistic in order to decide between detection and non-detection and also to relate our cross-correlation measurement to a physical quantity. Note that the expression for variance below neglects the contribution of gravity to the strain noise – our analysis is conducted in a weak signal limit.

$$\langle Y \rangle \equiv T \int_{-\infty}^{\infty} \tilde{Q}^*(f) \left\langle \tilde{h}^*(f) \tilde{h}(f) \right\rangle \mathrm{d}f \tag{1.9}$$

$$\approx \frac{T}{2} \lambda' \int_{-\infty}^{\infty} \frac{|S_{\rm gw}(f)|^2}{P_1(f) P_2(f)} \mathrm{d}f \tag{1.10}$$

$$\langle \tilde{h}^*(f') \tilde{h}(f) \rangle = \frac{1}{2} \delta_T(f-f') \tag{1.11}$$

$$\sigma_Y^2 \equiv \frac{T}{4} \int_{-\infty}^{\infty} |\tilde{Q}(f)|^2 P_1(f) P_2(f) \, \mathrm{d}f \tag{1.12}$$

$$\approx \frac{T}{4}\lambda'^2 \int_{-\infty}^{\infty} \frac{|S_{\rm gw}(f)|^2}{P_1(f)P_2(f)}\,{\rm d}f \tag{1.13}$$

The SNR (signal to noise ratio) will be maximized for the Wiener filter, $\tilde{Q}(f)$, that most accurately matches the stochastic gravitational wave background. That SNR will be given by:

$$\text{SNR} = \frac{\langle Y \rangle}{\sigma_Y} \approx \sqrt{T}\left[\int_{-\infty}^{\infty} \frac{|S_{\rm gw}(f)|^2}{P_1(f)P_2(f)}{\rm d}f\right]^{1/2}. \tag{1.14}$$

1.4.2 Non-trivial geometry

The overlap reduction function, $\gamma(f)$ quantifies the geometric loss in sky-averaged stochastic sensitivity experienced by two detectors that are not co-located and co-aligned. This definition ensures that co-located and co-aligned interferometers have an overlap reduction function of 1 at all frequencies (4/3 for bar detectors). If we were to begin with two co-located and co-aligned detectors and moved them apart, we would introduce a source location-dependent phase difference between the received signals. Averaging over an radiation from every point in the sky, there is destructive interference from the phase differences, resulting in a decrease in sensitivity. If we were to rotate them away from co-alignment, the detectors would be sensitive to different polarizations.

For plots of overlap reduction functions between pairs of interferometer sites from {LIGO Hanford, LIGO Livingston, GEO-600, TAMA-300, and Virgo}, see Appendix B of Allen and Romano[5]. In figure 1-6 below, we plot the overlap reduction functions of H1-H2 and H1-L1, the latter having provided the best upper limits to date.

The overlap reduction function will give H1-H2 the better stochastic sensitivity integrand ($\gamma_{\rm H_1L_1}/P_{\rm L_1} < \gamma_{\rm H_1H_2}/P_{\rm H_2}$), and that potential sensitivity should motivate us to enable them. Still, we should be cautious that better sensitivity may not be realized in the final analysis if we veto most of the sensitive frequencies, and which frequencies are sensitive is determined by the source spectrum for which we are searching. From figure 1-6, we can say immediately that for high frequency searches, using H1-H2 is

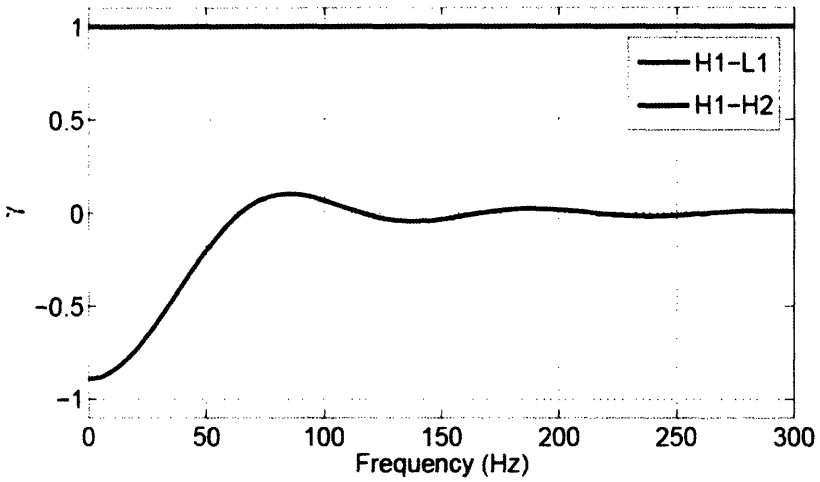

Figure 1-6: H1-L1 and H1-H2 overlap reduction functions. Above 300Hz, the H1-L1 overlap reduction function is essentially zero while the H1-H2 overlap reduction function remains at one.

absolutely essential.

Chapter 2

Identifying Environmental Correlation in H1-H2

2.1 Introduction

One real-world issue we did not address in the first chapter is that of common environmental noise. When we integrate a cross-correlation between two gravitational wave detectors, we actually obtain $\Omega_{\text{eff}} = \Omega_{\text{gw}} + \Omega_{\text{instr}}$. Ω_{eff} is comprised of a true gravitational signal and a signal which stems from non-gravitational correlations between the instruments. Ω_{instr} is particularly dangerous to an upper limit in Ω_{gw} in that it can be positive or negative (from correlated or anti-correlated signals), whereas Ω_{gw} must be positive.

For the case of H1-L1, a few narrow-band sources of inter-site correlation have been measured, such as the 1Hz comb that we believe stems from the GPS timing pulses[7][9]. However, having a phenomenon to which we can attribute these correlations, we can remove them. Careful estimates and measurements lead us to believe that other non-gravitational, inter-site correlations are well below the sensitivity of our search, so we take Ω_{instr} to be negligible and the measurement of Ω_{eff} to be a direct measurement of Ω_{gw}[23]. The H1-H2 pair, however, has known and unknown, broad- and narrow-band sources of common environmental noise.

There are two analysis approaches to dealing with the common environmental

noise. The first, more ideal solution is to regress out environmental correlations[6]. The regression technique is delicate in that it can introduce new cross-correlations if applied with insufficient care; its implementation is in the early stages of testing. We describe a second, less ambitious approach – identify frequencies at which environmental correlations are significant and exclude them from the stochastic search. As we shall see, while this method is still being explored, its results are promising and its implementation straightforward.

In section 2.2, we review practical knowledge of coherence, then examine H1-H2 coherence during LIGO's fourth science run (S4). Section 2.3 derives a relation between interferometer-interferometer coherence and interferometer-environmental coherences. We apply this relation in section 2.4, where we describe an algorithm which can identify frequency regions with high environmental correlations. In the results section, section 2.5, we demonstrate a significantly cleaner S4 H1-H2 coherence spectrum.

2.2 Coherence

To quantitatively characterize correlation, environmental or otherwise, we require a metric. Coherence is a frequency-domain measure of correlation independent of the spectral shape of the instruments' noise. However, coherence assumes stationary processes with constant couplings. If the noise is of a transient nature or the coupling changes over time, coherence is not a good measure. We should use coherence with these caveats in mind.

A coherence spectrum, denoted $\Gamma_{XY}(f)$, is the absolute square of the cross power spectral density (CPSD) between the two channels of interest, normalized by the individual power spectral densities (PSDs) of the channels. It is the absolute square of a complex-valued quantity and is guaranteed to be between zero and one at each frequency:

$$\Gamma_{XY}(f) = |\gamma_{XY}(f)|^2 = \frac{|P_{XY}(f)|^2}{P_{XX}(f)P_{YY}(f)}. \tag{2.1}$$

To estimate the coherence with a finite stretch of data, we use Welch's periodogram method. How we choose to segment the data to form periodograms has ramifications for our estimation of the coherence. The frequency resolution, Δf, is the reciprocal of the length of each data segment. The level of the coherence statistical noise floor (the expectation value of coherence for channels uncorrelated at a given frequency) is the reciprocal of the number of periodogram averages, N, which is inversely proportional to segment length. In summary, by increasing segment length, we improve the frequency resolution while increasing the noise floor.

Figure 2-1 shows the coherence between H1 and H2's gravitational strain channels as measured over the course of S4. If the interferometers were perfectly insulated from their common environment and the gravitational wave signature were below detectability, we would observe no major excursions from the noise floor (figure 2-1) and the coherence values would be exponentially distributed (figure 2-2). We expect a real gravitational background signature to be fairly broad, unlike many of figure 2-1's features. Furthermore, we can be sure that weak gravitational waves would not couple to any of our environmental monitors.

2.3 Environmental contributions to coherence

We would like to learn how the environment contributes to IFO-IFO (interferometer-interferometer) coherence. With this relation, we will estimate IFO-IFO coherence based on IFO-PEM (interferometer-physical environmental monitor) coherences. We can then set a simple threshold decision rule to identify contaminated frequencies.

The LIGO Hanford site has approximately 100 PEM sensors scattered throughout the facility, such as thermometers, wind sensors, seismometers, accelerometers, magnetometers, microphones, radio antennae and voltage monitors. However, thermometers and wind sensors are omitted from our analysis because they have very low sampling rates and frequencies below 40 or 50Hz are dominated by seismic disturbances; they would not provide any new information.

Let us derive the contribution to H1-H2 coherence from environmental couplings.

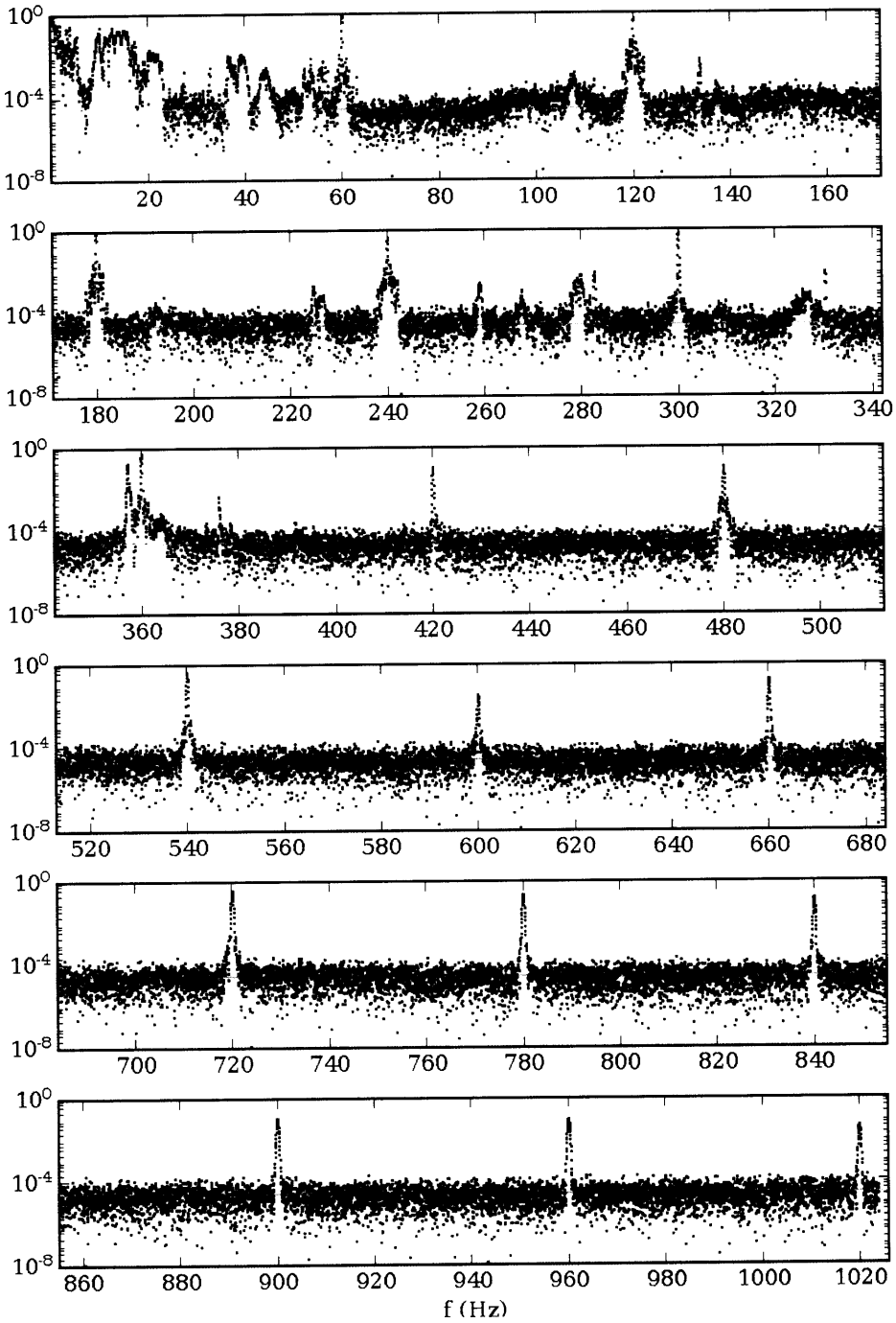

Figure 2-1: Reference coherence between H1 and H2 gravitational wave channels integrated over S4, $\Delta f = 1/32$Hz, $N_{\rm ref} = 3.7 \times 10^4$. Note the high coherence features, both narrow and broad. The horizontal line represents $1/N_{\rm ref} = 2.7 \times 10^{-5}$, the statistical noise floor.

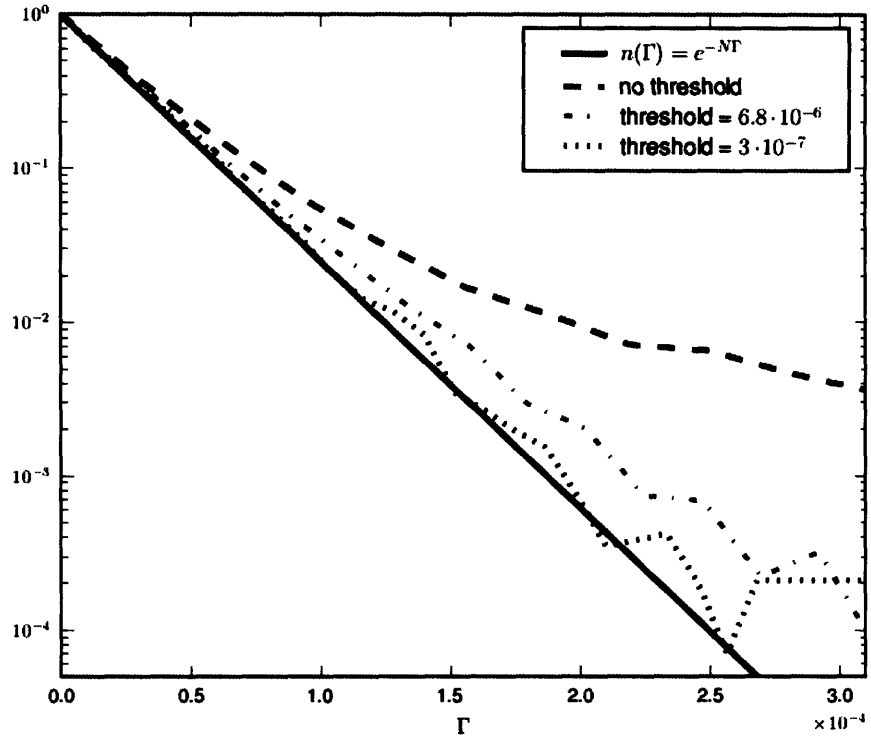

Figure 2-2: Histograms of bin-by-bin coherence values averaged over all of S4. The thick, solid line represents the expected distribution of Γ values if the two data streams were uncorrelated. The remaining lines show histograms of coherence from real data, with the veto threshold indicated by the legend. In all cases, the 0.1Hz band surrounding injected pulsars and the 5Hz band surrounding each 60Hz harmonic were vetoed.

We assume a *linear* channel model. X and Y are the channels of interest, i.e. H1 and H2 interferometer differential strain channels, and $Z_i(f)$ are channels which might cross-talk into $X(f)$ and $Y(f)$, i.e. PEM channels, and do not couple to gravitational waves. These $Z_i(f)$ will couple into X and Y with transfer functions $\alpha_i(f)$ and $\beta_i(f)$, respectively. $G(f)$ represents the true gravitational signal, which appears only between $X(f)$ and $Y(f)$, with respective coupling constants $\alpha_G(f)$ and $\beta_G(f)$. $n_X(f)$ and $n_Y(f)$ are noise terms, intrinsic to each detector, and statistically independent of one another.

$$
\begin{aligned}
X(f) &= \alpha_G(f)G(f) + \sum_i \alpha_i(f)Z_i(f) + n_X(f) \\
Y(f) &= \beta_G(f)G(f) + \sum_i \beta_i(f)Z_i(f) + n_Y(f) \\
P_{GZ_i} &= 0, \quad P_{n_X n_Y} = 0.
\end{aligned} \tag{2.2}
$$

There are a large number of environmental disturbances that could couple to the interferometers. They are generally not orthogonal, so there are cross-terms in decomposing γ_{XY} into its constituent signals (henceforth, explicit frequency dependence will not be denoted, but should be understood). The full, analytical expression for the coherence between X and Y is then:

$$
\gamma_{\text{instr}} \equiv \gamma_{XY}|_{G\to 0} = \frac{\sum_{i,j} \alpha_i^* \beta_j P_{Z_i Z_j}}{\sqrt{P_{XX} P_{YY}}}. \tag{2.3}
$$

It takes only a few lines of derivation to show that we can equate γ_{instr}, the instrumental component of H1-H2 IFO-IFO coherence, with a quantity composed of purely IFO-PEM and PEM-PEM coherences. In the following, $\cdot^{-1}$ denotes matrix inversion.

$$
\gamma_{XZ_i} = \frac{\sum_k \alpha_k^* P_{Z_k Z_i}}{\sqrt{P_{XX} P_{Z_i Z_i}}} = \sum_k \alpha_k^* \gamma_{Z_k Z_i} \sqrt{\frac{P_{Z_k Z_k}}{P_{XX}}} \tag{2.4}
$$

$$
\gamma_{Z_j Y} = \frac{\sum_l \beta_l P_{Z_j Z_l}}{\sqrt{P_{Z_j Z_j} P_{YY}}} = \sum_l \beta_l \gamma_{Z_j Z_l} \sqrt{\frac{P_{Z_l Z_l}}{P_{YY}}} \tag{2.5}
$$

$$
\sum_{i,j} \gamma_{XZ_i} \gamma^{-1}_{Z_i Z_j} \gamma_{Z_j Y} = \sum_{i,j,k,l} \alpha_k^* \beta_l \gamma_{Z_k Z_i} \gamma^{-1}_{Z_i Z_j} \gamma_{Z_j Z_l} \sqrt{\frac{P_{Z_k Z_k} P_{Z_l Z_l}}{P_{XX} P_{YY}}} \tag{2.6}
$$

$$
= \sum_{k,l} \alpha_k^* \beta_l \gamma_{Z_k Z_l} \sqrt{\frac{P_{Z_k Z_k} P_{Z_l Z_l}}{P_{XX} P_{YY}}} \tag{2.7}
$$

$$
= \frac{\sum_{k,l} \alpha_k^* \beta_l P_{Z_k Z_l}}{\sqrt{P_{XX} P_{YY}}} \tag{2.8}
$$

$$\therefore \Gamma_{\text{instr}} \equiv |\gamma_{\text{instr}}|^2 = \left| \sum_{i,j} \gamma_{XZ_i} \gamma^{-1}_{Z_i Z_j} \gamma_{Z_j Y} \right|^2 \tag{2.9}$$

For a real world situation where we have a finite and incomplete coverage of the environment, $i, j = 1..N$. Furthermore, there are nonlinear couplings in the system, which are not encapsulated in our model (see section 2.4.3). The best we can do is the following, where $\widehat{\cdot}$ denotes measurement:

$$\Gamma_{\text{instr}} \approx \left| \sum_{i,j=1..N} \widehat{\gamma}_{XZ_i} \widehat{\gamma}^{-1}_{Z_i Z_j} \widehat{\gamma}_{Z_j Y} \right|^2 . \tag{2.10}$$

The $\widehat{\gamma}_{Z_i Z_j}$ matrix is Hermitian and every diagonal element is 1, so with N channels, we must compute $N(N-1)/2$ matrix elements, which requires $N(N-1)/2$ PEM-PEM coherence calculations. Additionally, for Γ_{instr}, we require $2N$ IFO-PEM coherence calculations and as many $N \times N$ matrix inversions as there are frequency bins. For our system, however, it turns out that we can do almost as well with just the $2N$ IFO-PEM coherence calculations. Many channels are almost entirely redundant in the information they convey ($Z_i(f) \approx aZ_j(f)$ for some a, possibly $a = 0$), especially within a given narrow frequency band. Seismometers and accelerometers are highly correlated below 40 to 50Hz; at 60Hz harmonics, all of the channels exhibit a coherent peak due to power mains.

Let us assume that at each frequency, there is a single, dominant, physical underlying phenomenon. Multiple reports of the same phenomenon do not add much new information. Furthermore, other quiet channels do not add much new information. Because of channel redundancies and nearly zero rows and columns, the matrix $\widehat{\gamma}_{Z_i Z_j}$ is then almost singular and the inverse is difficult to compute numerically. We sidestep the matrix inversion issue by removing all dominant channels but one, the most dominant, and removing non-dominant channels, which we believe do not contribute. By removing these channels' corresponding rows and columns from the PEM-PEM coherence matrix $\widehat{\gamma}$ (with elements $\widehat{\gamma}_{Z_i Z_j}$), we remove the almost-singularity and happen to leave behind a 1×1 matrix, $\widehat{\gamma'}$, whose only element's value is known since self-coherence is always 1: $\widehat{\gamma'} = (1)$. Therefore, $\widehat{\gamma'}^{-1} = (1)$. Equation 2.10 reduces to

$\Gamma_{\text{instr}} \approx |\widehat{\gamma}_{XZ_i}\widehat{\gamma}_{Z_iY}|^2$ for the index i corresponding to the dominant channel. We interpret the most dominant channel to be that with the greatest contribution to Γ_{instr}. Therefore, for each separate frequency bin:

$$\Gamma_{\text{instr}} \approx \max_i |\widehat{\gamma}_{XZ_i}\widehat{\gamma}_{Z_iY}|^2 = \max_i \widehat{\Gamma}_{XZ_i} \cdot \widehat{\Gamma}_{Z_iY} \tag{2.11}$$

Equation 2.11 is motivated by our knowledge that our system has many channels which provide nearly redundant information. After applying the above rank-reduction scheme, there are N candidate channels over which to maximize, each of which requires 2 coherence calculations. Requiring only $2N$ coherences makes the approximation practical to compute over all available PEM channels and over very long data sets. Having an estimate for $\Gamma_{\text{instr}}(f)$, we can now set a threshold on the maximum coherence contribution we want from the environment, within the error of our estimate. We exclude from the stochastic search all frequencies for which $\Gamma_{\text{instr}}(f)$ exceeds this threshold.

2.4 Implementation

With our simple approximation, we can design a computer program to flag regions of high environmental correlation. With this knowledge, the stochastic search can ignore contaminated frequencies. Figure 2-3 shows the basic structure of one such implementation. In summary, we compute IFO-PEM coherences, multiply spectra, and take the bin-by-bin maximum across channels. The resulting spectrum is then thresholded to provide frequency vetoes. The following subsections describe design choices and the data set over which we provide initial checks of the method.

2.4.1 Degrees of Freedom

In generating vetoes, we must choose a data set, a set of channels, a frequency resolution, and a threshold. The question of threshold is important and is the topic of section 2.4.2. This section describes the other choices made in conducting the

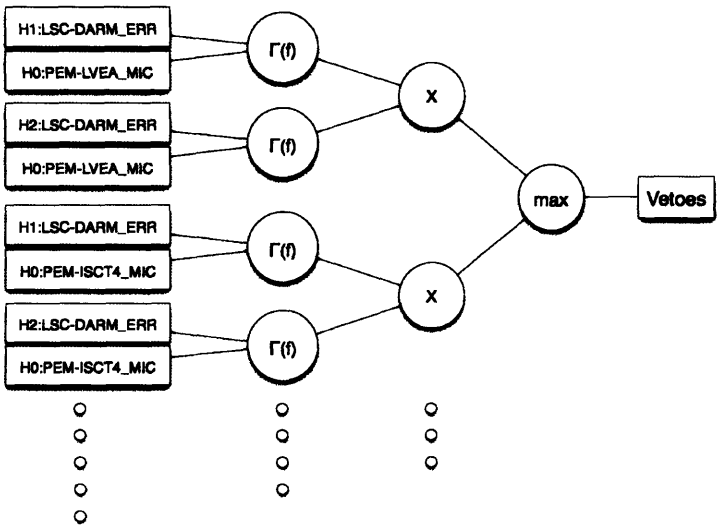

Figure 2-3: Flowchart of our H1-H2 frequency veto generator. Data flows from left to right. `Hn:LSC-DARM_ERR` are the gravitational wave channels and `H0:PEM-XXXX_MIC` are examples of microphone channels. $\Gamma(f)$ denotes taking the coherence between the two input channels, `x` denotes bin-by-bin multiplication, and max denotes taking the maximum across PEM channels.

analysis.

In the test and validation of the technique described here, we use IFO-PEM coherences that had been previously computed for use in line-finding and other detector characterization work, as the computation is rather intensive. This data set is a very conservative subset of S4 data that excludes all segments marked as having a data quality issue. H1-PEM coherences are computed with all surviving H1 segments, and H2-PEM coherences are computed with all surviving H2 segments. The frequency resolution is 0.01Hz. These parameters determine the length and number of segments analyzed to be 100 seconds and $N \approx 1.3 \times 10^4$, respectively.

To help us gauge success, we test against a reference H1-H2 coherence measurement to represent the response of the stochastic search to vetoes. We must also choose data set and frequency resolution for this reference. Ideally, we would like these reference parameters to match the IFO-PEM parameters, with both matching the parameters that would be used in a real stochastic search. In this trial study, however, the IFO-PEM parameters do not match what we would use for the stochastic search. Nonetheless, we choose to make the reference H1-H2 coherence measurement

with the stochastic search's data set and frequency resolution. We use a subset of H1-H2 coincident data in S4 that removes data known to be compromised due to instrumental problems or otherwise taken during anomalously strong environmental disturbances. The stochastic search uses a frequency resolution of 1/32Hz. These choices set the length and number of segments to be 32 seconds and $N_{\text{ref}} \approx 3.7 \times 10^4$, respectively.

2.4.2 Threshold

There are two bounds between which we should place our threshold. The upper limit is the $1/N_{\text{ref}}$ noise floor of the reference coherence. If correlation above this level is obvious in coherence, it seems likely that it could impact the stochastic search. Naively, we should set a threshold to some level at or below this. The lower limit on threshold is the $1/N^2$ floor, which is naively the expectation value of the PEM coherence products; if we set the threshold below that, we have no remaining data to analyze. Actually, the "$1/N^2$" noise floor will be somewhat higher than $1/N^2$, since we are taking the maximum across 100 cproducts, each product being composed of 2 independent random factors, each factor being drawn from an exponential distribution.

We have not yet developed a solid metric other than coherence for directly assessing environmental contamination, so the final choice is somewhat arbitrary at this point. We have chosen two thresholds with which to evaluate this technique, one at 6.8×10^{-6}, which is a factor of 4 below the stochastic search's $1/N_{\text{ref}}$ level, and 3×10^{-7}, which we estimate is as low as we can set the threshold without cutting bins that are definitely uncorrelated. Without formal calculations, these thresholds seem reasonable. In the future, it may be possible to determine how to set our threshold such that we maximize our stochastic sensitivity subject to a maximum environmental contribution to Ω_{eff}, either analytically or via simulation.

2.4.3 Caveats

Let us consider what circumstances might confound our implementation in the real world. Prominent considerations include possible false positives and false negatives. False positives can occur primarily when the threshold is chosen to be below $1/N$ due to the $1/N$ noise floor of the individual coherences. For instance, if the coherence between the H1 differential strain channel and a microphone at 371Hz were 0.95 and if the H2 differential strain channel and the same microphone were totally uncorrelated, then we would measure the 0 coherence as approximately $1/N$, so the coherence product would be $0.95/N$. A threshold below $0.95/N$ would then incorrectly assert that H1 and H2 are coherent due to acoustic couplings at 371Hz. This type of misidentification is not dangerous to the stochastic search per se, but results in a loss of data.

False negatives, or misses, will contribute toward Ω_{instr}. There are several reasons we might not be able to identify frequencies that are coupled to the environment. Of course, there is the question of whether our approximation is valid – is there really one dominant physical source of correlation? Another is our choice of threshold – have we removed enough correlation that Ω_{instr} becomes negligible? We will discuss this in the final section. Other contaminated regions we might accept as good are literally due to blind spots – what if we are just not monitoring some phenomenon in the environment that couples to the interferometers or are not monitoring near enough to the coupling site? This will always be a possibility. Finally, this technique cannot bound the coherence contribution from non-linear couplings. Further studies using bicoherence are necessary to better assess the effects of non-linearities.

2.5 Results

Figures 2-2, 2-4, 2-5, and 2-6 give the final results of this initial experiment. We find that we can identify nearly all regions of high H1-H2 coherence and the responsible physical coupling by looking only at coherence between the interferometers and environmental channels. The higher threshold does almost as well as the lower threshold,

as measured by the remaining coherence histogram of figure 2-2.

Looking at figure 2-4, the difference between the estimated coherence and the measured reference coherence appears very small everywhere above the $1/N$ line, demonstrating that equation 2.11 is a reasonable approximation. Not shown in this thesis, but manually verified, is that we see exactly the redundancy in the channels that we expect – a given coherent region would be vetoed individually in tens of channels and the coherence feature is notable in many others.

With the higher threshold of 6.8×10^{-6}, the coherence histogram shown in figure 2-2 has orders of magnitude fewer outliers than that of no threshold, but still contains several discrete deviations from expectation and systematically higher slope fall-off in the tail. Referring again to figure 2-5, it looks as if the discrete outliers come from the vicinity of 60Hz and that a large fraction of the tail might come from the vicinity of 90Hz. This threshold seems not to be low enough.

Lowering the threshold to 3×10^{-7}, the coherence histogram of figure 2-2 is yet better, with less excess over uncorrelated streams. Indeed, the histogram may be consistent within counting statistics to no correlation. We interpret this as evidence that there is sufficient information in our approximation to completely clean the coherence within our ability to measure. We will discuss more advanced metrics in chapter 5.

Between 50 and 350Hz, the most sensitive part of the instruments' range, 44% of frequency space was vetoed with a threshold of 6.8×10^{-6}, and 93% with the 3×10^{-7} threshold. Between 0 and 1024Hz, the total range of PEM coverage, 26% of frequencies were vetoed with a threshold of 6.8×10^{-6}, and 60% with the 3×10^{-7} threshold. As we ablate data, we erode H1-H2's advantage. Exactly how much depends on the stochastic sensitivity integrand at those frequencies. Unfortunately, we are primarily vetoing the lower frequencies, which are the most important in searching for a flat stochastic background. While we still have to evaluate what threshold is most appropriate, it is not clear yet whether or not H1-H2 will have greater stochastic sensitivity than H1-L1 after vetoes.

An important result is that we have determined frequencies above roughly 420Hz

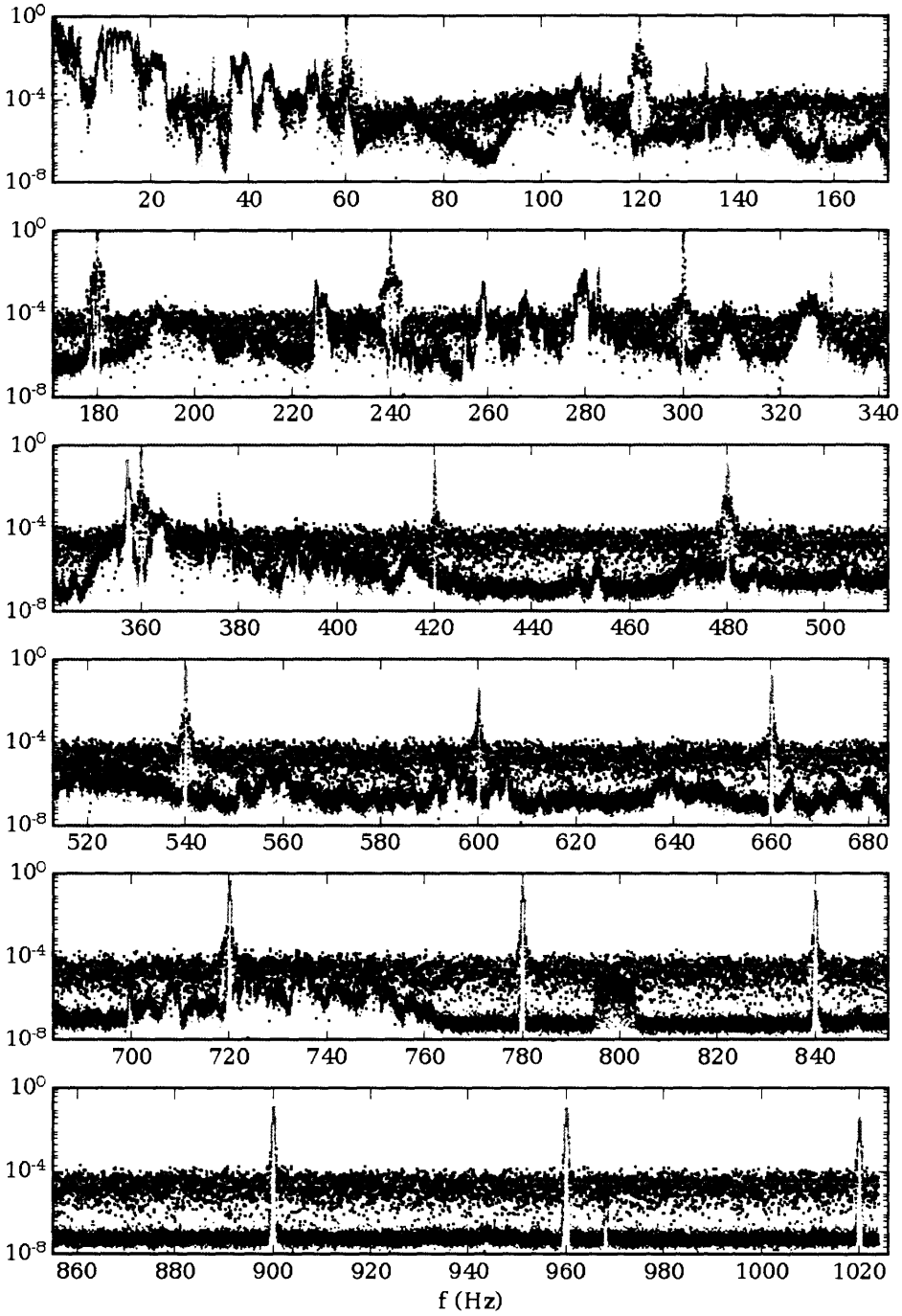

Figure 2-4: H1-H2 coherence with coherence product max. The upper, black dots are H1-H2 coherence with 1/32Hz frequency resolution and the horizontal line is $1/N_{\text{ref}} \approx 2.7 \times 10^{-5}$. The lower, gray dots are the IFO-PEM coherence product maxima with 1/100Hz frequency resolution and $1/N^2 \approx 10^{-8}$.

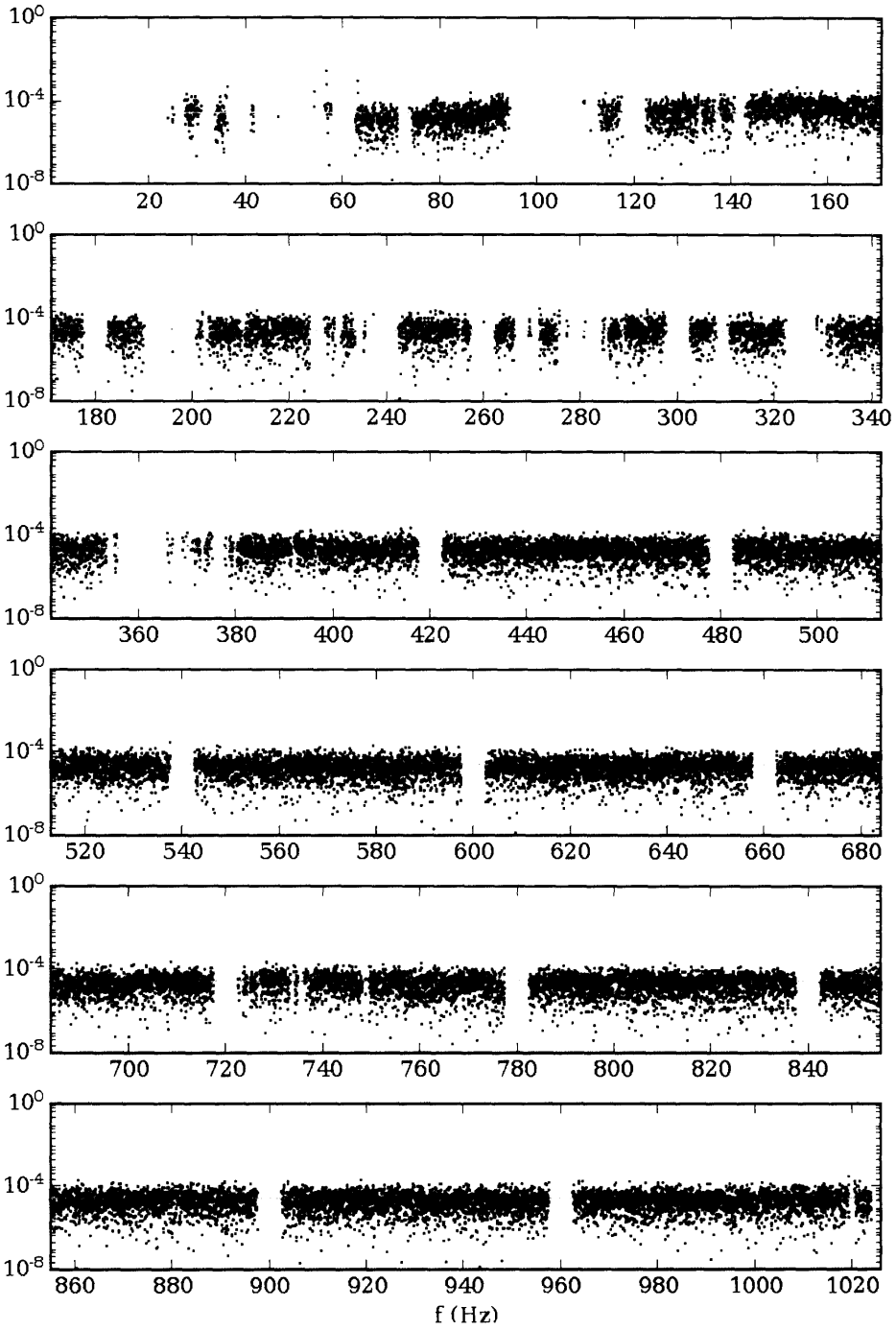

Figure 2-5: H1-H2 coherence with frequency vetoes, threshold=6.8×10^{-6}. The broken series of points is H1-H2 coherence with 1/32Hz frequency resolution and $1/N_{\mathrm{ref}} \approx 2.7 \times 10^{-5}$. Only frequency bins surviving the veto threshold of 6.8×10^{-6} are displayed. Additionally, the 0.1Hz band surrounding injected pulsars and the 5Hz band surrounding each 60Hz harmonic were vetoed.

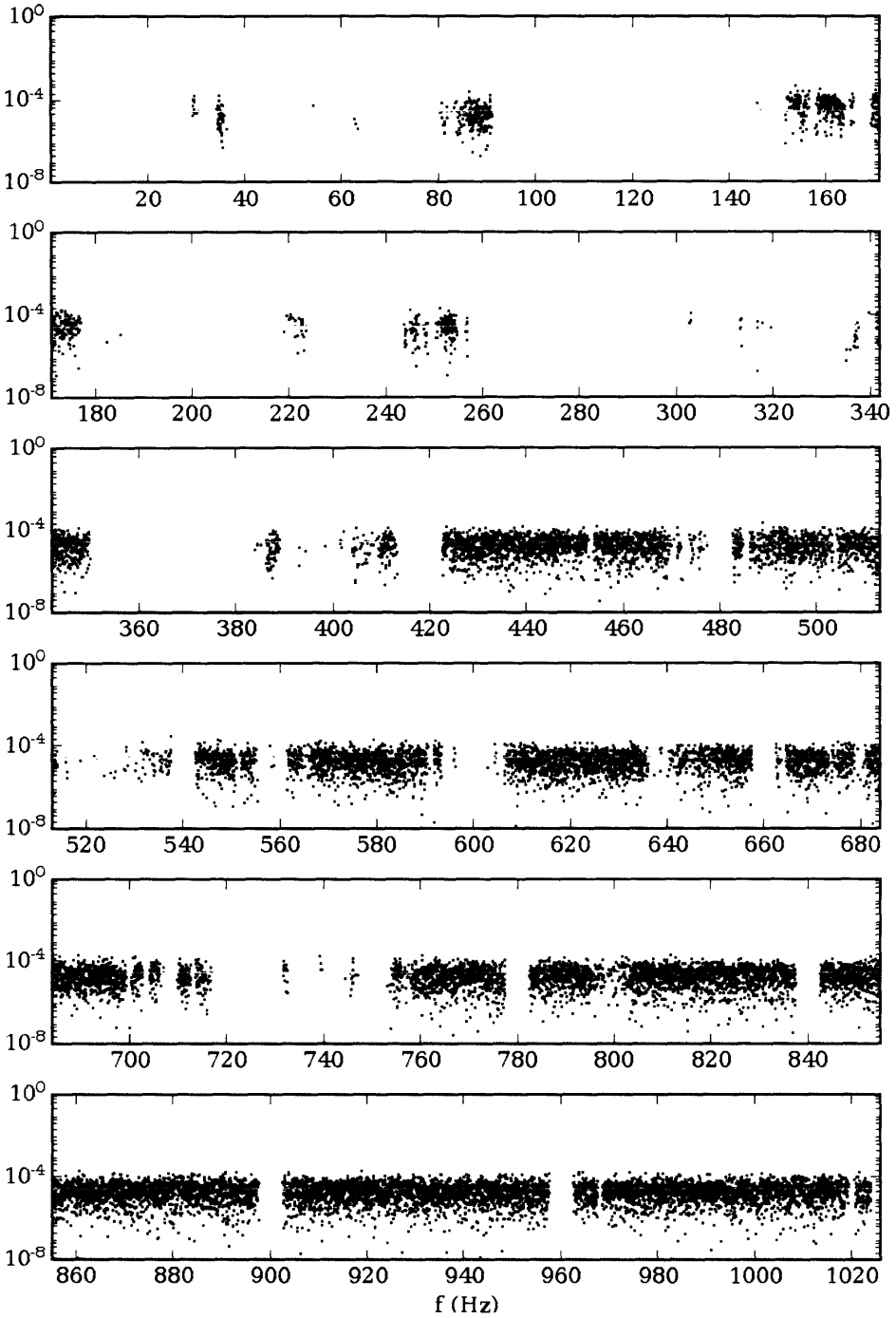

Figure 2-6: H1-H2 coherence with frequency vetoes, threshold=3×10^{-7}. The broken series of points is H1-H2 coherence with 1/32Hz frequency resolution and $1/N_{\text{ref}} \approx 2.7 \times 10^{-5}$. Only frequency bins surviving the veto threshold of 3×10^{-7} are displayed. Additionally, the 0.1Hz band surrounding injected pulsars and the 5Hz band surrounding each 60Hz harmonic were vetoed.

to be largely free of contamination, making it appealing to use H1-H2 for higher frequency searches for astrophysical sources of stochastic gravitational waves. This also has ramifications for planned cryogenic bar detectors, which typically have narrow sensitivity in the kilohertz region. Moreover, we have a useful detector characterization tool. For each vetoed bin, we know the dominant environmental coupling. Even if this technique does not succeed in its goal of enabling H1-H2 for trusted stochastic upper limits better than those of H1-L1, it is at least a sensitive diagnostic for improving the instruments.

Chapter 3

Modeling Astrophysical Gravitational Wave Spectra

The previous chapter laid out a technique to remove common noise between the LIGO Hanford instruments. With their relative geometry's improved sensitivity at high frequencies relative to H1-L1 and H2-L1, the H1-H2 pair grants us better opportunities to search for kilohertz-range astrophysical stochastic backgrounds.

To optimally search for the presence of a signal, we must perform Wiener filtering. To form the optimal filter of equation 1.7, we require models of the stochastic background's energy spectrum. This chapter will largely describe the methods and results of Regimbau and de Freitas Pacheco, which they use in several papers to predict $\Omega_{\rm gw}(f)$. Other authors use variations of the same idea. Source detectability is a major focus of most astrophysical papers on gravitational waves, but we will depart from them in that we care only about spectral shape and not amplitude.

3.1 General Technique

In order to obtain the amalgamated spectrum of a population of gravitational wave emitters, we need to know the average source's emitted spectrum, the distribution of these sources across space-time, and how radiation changes as it propagates through an expanding universe. We will assume that sources will radiate in the same way

at all eras, and adopt parameters for that radiation spectrum from observational averages. Let us relate $\Omega_{\rm gw}(\nu_{\rm o})$, the stochastic energy density spectrum as we measure at observation frequency $\nu_{\rm o}$, to the spectra of individual sources and their places in the universe.

$$\begin{aligned}
\Omega_{\rm gw}(\nu_{\rm o}) &\equiv \frac{1}{\rho_{\rm critical}}\frac{{\rm d}\rho_{\rm gw}}{{\rm d}\ln\nu_{\rm o}} && (3.1)\\
&\equiv \frac{8\pi G}{3H_0^2}\nu_{\rm o}\frac{{\rm d}\rho_{\rm gw}}{{\rm d}\nu_{\rm o}} && (3.2)\\
&= \frac{8\pi G}{3H_0^2c^3}\nu_{\rm o}\frac{{\rm d}(\rho_{\rm gw}c^2\cdot c)}{{\rm d}\nu_{\rm o}} && (3.3)\\
&\equiv \frac{8\pi G}{3H_0^2c^3}\nu_{\rm o}F_{\nu_{\rm o}} && (3.4)
\end{aligned}$$

We began with the definition of $\Omega_{\rm gw}(f)$ and expanded definitions. $\rho_{\rm critical} = 3H_0^2/(8\pi G)$ and ${\rm d}\rho_{\rm critical}/{\rm d}\ln\nu_{\rm o} = \nu_{\rm o}{\rm d}\rho_{\rm critical}/{\rm d}\nu_{\rm o}$. Then, we converted mass density, $\rho_{\rm gw}$, to the flux (erg·cm^{-2}·s^{-1}) from an energy density $\rho_{\rm gw}c^2$ moving at the speed of light, c. We are now left with a specific flux, $F_{\nu_{\rm o}}$ [erg·s^{-1}·Hz^{-1}·cm^{-2}] and prefactors.

Continuing,

$$F_{\nu_{\rm o}} = \int f_{\nu_{\rm o}}(z)\frac{{\rm d}R}{{\rm d}z}\,{\rm d}z. \qquad (3.5)$$

Here, we decompose the flux into the specific fluence from each source, $f_{\nu_{\rm o}}$ [erg·Hz^{-1}·cm^{-2}], integrated over the number of sources radiating per unit time per unit redshift, ${\rm d}R/{\rm d}z$ [s^{-1}·z^{-1}]. With this factorization, we have separated the spectra of individual sources from their distribution across space-time.

3.1.1 Source Fluence

Let us reduce the fluence from an individual source in equation 3.5 further. It will decompose naturally into an intrinsic source spectrum and a geometric factor.

$$f_{\nu_o}(z) = \frac{1}{4\pi d_L^2(z)} \left.\frac{dE_{gw}}{d\nu_o}\right|_{\nu=\nu_o(1+z)} \tag{3.6}$$

$$= \frac{1}{4\pi d_L^2(z)} \left.\frac{dE_{gw}}{d\nu}\right|_{\nu=\nu_o(1+z)} (1+z) \tag{3.7}$$

$$r(z) = \frac{c}{H_0}\int_0^z \frac{dz'}{E(z')}, \quad d_L(z) = r(z)(1+z), \quad E(z) = \sqrt{\Omega_m(1+z)^3+\Omega_\Lambda} \tag{3.8}$$

r, d_L, and $E(z)$ are conceptually useful cosmological functions; an excellent reference for these is by Hogg[18]. Ω_m and Ω_Λ represent the fractions of matter and dark energy, respectively, in the universe to the critical density. The specific fluence is the specific energy radiated from a source diluted over a sphere of area $4\pi d_L^2(z)$, where we've assumed isotropic radiation and $d_L(z)$ is the luminosity distance to the source. The redshift of the spectrum is taken into account by evaluating the specific energy at the blue-shifted observation frequency. A $d\nu_o/d\nu = 1+z$ factor allows us to use the $dE/d\nu$ function, which is the energy spectrum at the source and includes the total radiated gravitational wave energy from that source. It is assumed to be the same for all sources in a population. Now that we know how the fluence spectrum appears to us from any given source, let us consider how the sources are distributed throughout the universe.

3.1.2 Event Rate Density

On variables represented by R, the * superscript will denote mass per comoving volume per year, and its omission will denote number per unit redshift. In general, the gravitational wave event rate density, $R^*(z)$, can be related to the progenitor systems' formation rate density, $R_f^*(z)$. We will leave this relationship unspecified at the moment, as this varies from system to system. Let us relate $R_f^*(z)$ $[M_\odot \cdot s^{-1} \cdot Mpc^{-3}]$ with dR_f/dz $[s^{-1} \cdot z^{-1}]$:

$$\left.\frac{\mathrm{d}R_\mathrm{f}}{\mathrm{d}z}\right|_z = \frac{R^*_\mathrm{f}(z)}{1+z}\left.\frac{\mathrm{d}V}{\mathrm{d}z}\right|_z \tag{3.9}$$

$$\left.\frac{\mathrm{d}V}{\mathrm{d}z}\right|_z = 4\pi r(z)^2 \frac{c}{H_0}\frac{1}{E(z)}. \tag{3.10}$$

The factor of $1/(1+z)$ is $(d\tau/\mathrm{d}t)^{-1}$, where τ is the observer's proper time and t is the time as measured at the source. $\mathrm{d}V/\mathrm{d}z$ is the volume enclosed within a sphere of radius $r(z)$, per unit redshift. See equation 3.8 for the definitions of the cosmological quantities.

3.1.3 Summary

In summary, our population spectrum will be:

$$\Omega_\mathrm{gw}(\nu_\mathrm{o}) = \frac{8\pi G}{3H_0^3c^2}\nu_\mathrm{o}\int_{z_\mathrm{min}}^{z_\mathrm{max}} \frac{R^*(z)}{E(z)(1+z)^2}\left.\frac{\mathrm{d}E_\mathrm{gw}}{\mathrm{d}\nu}\right|_{\nu=\nu_\mathrm{o}(1+z)} \mathrm{d}z. \tag{3.11}$$

Invariably, the event rate density, $R^*(z)$, will somehow relate back to the star formation rate density, R^*_SFR. We use Porciani and Madau's fit for an $(\Omega_m = 1, \Omega_\Lambda = 0, h = 0.65)$ universe[24][1], R^*_PM, corrected for modern values $(\Omega_m = 0.3, \Omega_\Lambda = 0.7, h = 0.7)$:

$$R^*_\mathrm{SFR}(z) = \frac{h}{0.65}\frac{E(z)}{(1+z)^{3/2}}R^*_\mathrm{PM} \tag{3.12}$$

$$R^*_\mathrm{PM}(z) = 0.15\frac{e^{3.4z}}{22.+e^{3.4z}}. \tag{3.13}$$

We truncate the SFR at $z = 5$. The spectra are largely insensitive to where this cutoff lies.

Finally, we will often make use of the Salpeter initial mass function, $\xi(m) = Am^{-2.35}$. It models the mass distribution of newborn stars. $m\xi(m)$ is the probability

[1]Actually, Porciani and Madau provide a couple fits to GRB data which differ in various corrections at high redshift. The details of the SFR at high redshift do not strongly affect the spectra of this thesis, so we chose their SFR2 model.

density of star formation at a given mass. A is the unit normalization of $m\xi(m)$, which we take over the range $0.1M_\odot$ to $80M_\odot$.

Our population spectrum model is almost complete. Still needed are an individual source's radiation spectrum, $\mathrm{d}E/\mathrm{d}\nu$, and a relationship between the source population's event rate and their progenitors' formation rate. These are discussed on a source-by-source basis in the following sections of this chapter.

3.2 Search Models

In this section, we will derive the radiation spectra for various gravitational wave emitters. These systems were selected for having energy in frequencies accessible to LIGO's H1-H2 pair and for well understood spectral shapes. Again, accurately modeling the amplitude of the waveforms is not important for the purpose of performing Wiener filtering.

3.2.1 Pulsars

Over the course of its magnetic spin-down, a lone neutron star with a small ellipticity, ϵ, moment of inertia, I_{zz}, magnetic braking time-scale, τ_m, and initial period, P_0, will radiate the net radiation spectrum of [25][27][2]:

$$\frac{\mathrm{d}E_\mathrm{gw}}{\mathrm{d}\nu} = K\nu^3 = \frac{512\pi^6 G}{5c^5}\epsilon^2 I_{zz}^2 \frac{\tau_\mathrm{m}}{P_0^2}\nu^3. \tag{3.14}$$

Common assumptions for neutron star parameters are $\epsilon = 10^{-6}$ and $I_{zz} = 1.4 \times 10^{45}\,\mathrm{g{\cdot}cm^2}$. Regimbau and de Freitas Pacheco have estimated $\left\langle \frac{\tau_\mathrm{m}}{P_0^2} \right\rangle = 3.7 \times 10^{13}\,\mathrm{s}^{-1}$ via Monte Carlo simulation. The spectrum only holds in the (emitted) frequency band $[0, \nu_\mathrm{K}]$, where we take the initial Keplerian frequency to be $\nu_\mathrm{K} =$ 2500Hz.

Neutron stars are born from relatively massive stars, probably between $10M_\odot$ and $40M_\odot$, who consume their nuclear fuel quickly in cosmic time. We can therefore take

[2]There is a factor of 2 missing from the equation given in [27].

the neutron star formation rate to be proportional to the cosmic star formation rate:

$$R^*_{\rm NS} = \lambda_{\rm NS} R^*_{\rm SFR}. \tag{3.15}$$

Using the Salpeter initial mass function, we obtain the neutron star progenitor mass fraction $\lambda_{\rm NS} = \int_{10M_\odot}^{40M_\odot} \xi(m)\,{\rm d}m = 4.8 \times 10^{-3} M_\odot^{-1}$. Therefore, the final contribution due to $\Omega_{\rm gw}$ due to solitary pulsars is:

$$\Omega_{\rm NS}(\nu_{\rm o}) = \left(\frac{8\pi G}{3H_0^2 c^3}\frac{h}{0.65}\right)\left(\frac{512\pi^6 G}{5c^5}\epsilon^2 I_{zz}^2 \frac{\tau_{\rm m}}{P_0^2}\right)\lambda_{\rm NS}\,\nu_{\rm o}^4 \int_{z_{\rm min}}^{z_{\rm max}} \frac{R^*_{\rm PM}(z)}{(1+z)^{1/2}}{\rm d}z. \tag{3.16}$$

One final matter is that of the limits of integration. $z_{\rm min}$ we can set to 0 since pulsars are continuous emitters and we do not have to worry about duty cycle and its ramifications. $z_{\rm max}$ is capped by the Keplerian frequency, $\nu_{\rm K}$. For each observation frequency, $\nu_{\rm o}$, there is a redshift $z_{\rm max}$ beyond which the maximum emitted frequency, $\nu_{\rm K}$, redshifts below $\nu_{\rm o}$. Another limit is that there is no star formation past about $z = 5$. We encode these physical constraints by setting:

$$z_{\rm max} = \min\left\{\frac{2500{\rm Hz}}{\nu_{\rm o}} - 1, 5\right\} \tag{3.17}$$

Performing numerical integration on $\Omega_{\rm NS}(\nu_{\rm o})$, we obtain the pulsar population's gravitational wave spectrum in figure 3.2.1

3.2.2 Magnetars

Magnetars have the same gravitational radiation emission mechanism as standard pulsars – while the neutron star is spinning down due to magnetic effects, they will continuously emit gravitational radiation. The difference appears in that the magnetic field is now strong enough to significantly deform the neutron star's shape. The degree of deformation depends on the magnetic field geometry, the equation of state, and whether or not the core is superconducting, but in general, the energy radiated per source is much greater[28]. At the same time, there are far fewer magnetars than

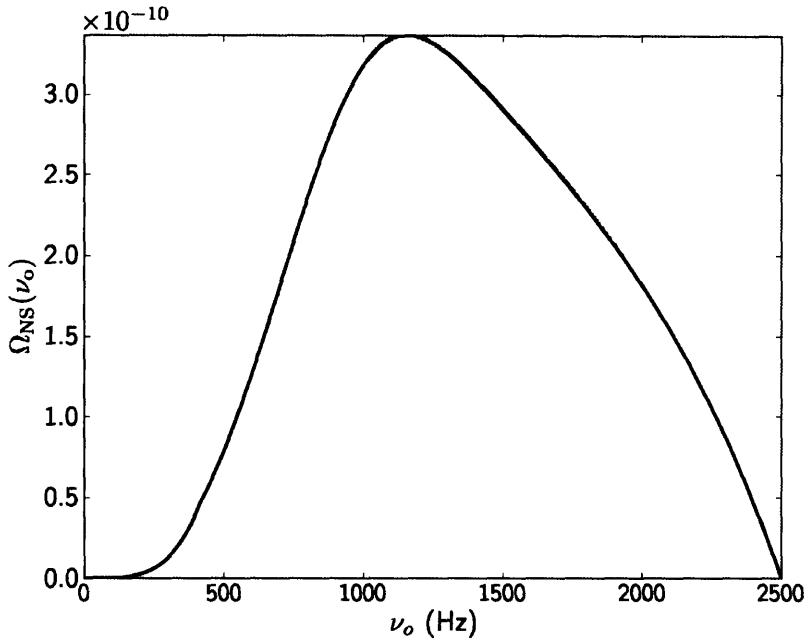

Figure 3-1: Expected stochastic gravitational wave background due to pulsars spinning down throughout the universe. Magnetar spindowns will have the same spectral shape, but an amplitude 10× greater.

other pulsars. The spectrum is $\sim$ 10× larger than the pulsar spectrum, but the uncertainties are also substantially greater.

As the magnetar spectrum is identical to the pulsar spectrum up to overall scaling, no separate search is necessary.

3.2.3 Black Hole Ringdowns

Once their nuclear fuel is spent, some sufficiently massive stars will undergo core-collapse and supernova, leaving behind a black hole. This violent process radiates copiously in gravitational waves. While the process can be simulated in full GR and the full spectrum can be calculated[30], the majority of energy is radiated in quasi-normal mode (QNM) perturbations of the spacetime metric. We follow the simpler computation of Tania Regimbau[25], which assumes that all energy is radiated at the lowest-order QNM frequency.

As the QNM frequency is determined by the mass and each emitter will not be

the same, we cannot use a single $\lambda_{\rm p} {\rm d}R_{\rm f}/{\rm d}z$ as before. Instead, we will incorporate the mass information via a ${\rm d}R_{\rm f}/{\rm d}z{\rm d}m$, then integrate over the mass range of stars that eventually collapse to black holes.

$$\frac{{\rm d}E_{\rm gw}}{{\rm d}\nu} = \epsilon\alpha m c^2 \delta(\nu - \nu_*(m)) \tag{3.18}$$

$$\frac{{\rm d}R_{\rm f}(z)}{{\rm d}z{\rm d}m} = \xi(m)\frac{R^*_{\rm SFR}(z)}{1+z}\frac{{\rm d}V}{{\rm d}z} \tag{3.19}$$

$$\nu_*(m) = \Delta\frac{1M_\odot}{\alpha m} \tag{3.20}$$

m is the progenitor mass. α is the fraction of the progenitor mass that goes into the black hole, which we take to be 0.2. ϵ is the fraction of black hole mass converted to gravitational waves, which we approximate with $\epsilon \approx 10^{-4}$. Δ is the frequency of the lowest-order QNM for a $1M_\odot$ black hole, which has been calculated as $\Delta \approx 12$kHz, and $\nu_*(m)$ is the frequency of the lowest-order QNM for a black hole of arbitrary mass. $\xi(m) = Am^{-2.35}$ is our familiar Salpeter initial mass function, and we again use the cosmic star formation rate, as black hole progenitors are very massive and collapse quickly, so the star formation rate has not changed appreciably between formation and collapse times. Using this information:

$$\Omega_{\rm gw}(\nu_{\rm o}) = \frac{8\pi G}{3H_0^2c^3}\nu_{\rm o}F_{\nu_{\rm o}} \tag{3.21}$$

$$F_{\nu_{\rm o}} = \int_{z_{\rm min}(\nu_{\rm o})}^{z_{\rm max}(\nu_{\rm o})}\int_{40M_\odot}^{80M_\odot}\frac{c}{H_0}\frac{\xi(m)R^*_{\rm SFR}(z)}{(1+z)^2E(z)}\left.\frac{{\rm d}E_{\rm gw}}{{\rm d}\nu}\right|_{\nu=\nu_{\rm o}(1+z)}{\rm d}m\,{\rm d}z \tag{3.22}$$

$$= A\alpha c^2\frac{c}{H_0}\left(\frac{\alpha}{\Delta}\right)^{0.35}\frac{h}{0.65}\nu_{\rm o}^{-0.65}\int_{z_{\rm min}(\nu_{\rm o})}^{z_{\rm max}(\nu_{\rm o})}\frac{R^*_{\rm PM}(z)\,{\rm d}z}{(1+z)^{4.15}} \tag{3.23}$$

$$\Omega_{\rm gw}(\nu_{\rm o}) = \frac{8\pi G}{3H_0^3}A\alpha\left(\frac{\alpha}{\Delta}\right)^{0.35}\frac{h}{0.65}\nu_{\rm o}^{0.35}\int_{z_{\rm min}(\nu_{\rm o})}^{z_{\rm max}(\nu_{\rm o})}\frac{R^*_{\rm PM}(z)\,{\rm d}z}{(1+z)^{4.15}} \tag{3.24}$$

The redshift limits of integration are determined by the QNM frequencies of $40M_\odot$ and $80M_\odot$ black hole progenitors. At low enough observation frequencies, even $80M_\odot$ progenitor-mass black holes will have QNM frequencies too high to observe at $z = 5$.

Conversely, at high observation frequencies, even $40M_{\odot}$ progenitor-mass black holes will have QNM frequencies too low to observe at $z = 0$. We can codify these bounds as:

$$z_{\min}(\nu_o) = \max\left\{\frac{750\text{Hz}}{\nu_o} - 1, 0\right\} \tag{3.25}$$

$$z_{\max}(\nu_o) = \min\left\{\frac{1500\text{Hz}}{\nu_o} - 1, 5\right\} \tag{3.26}$$

The model can be numerically integrated to produce the spectrum of figure 3-2.

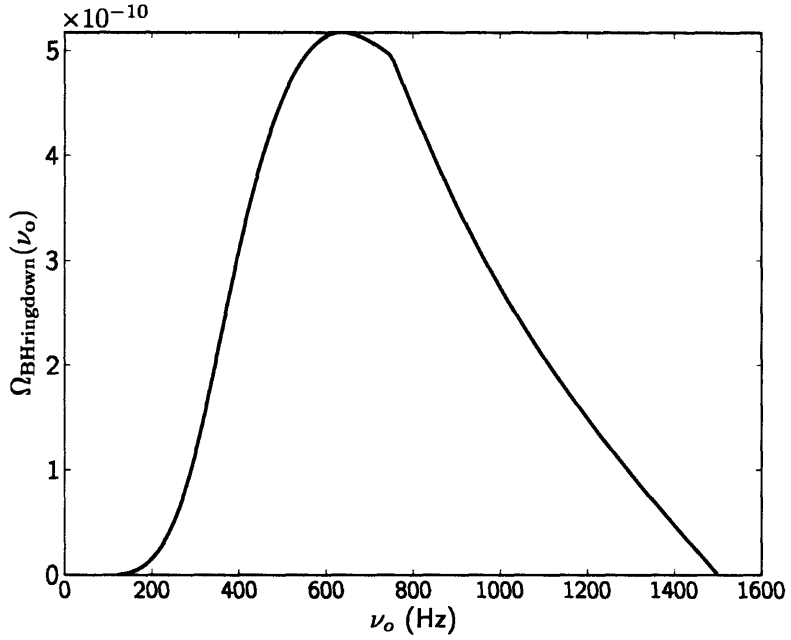

Figure 3-2: Expected stochastic gravitational wave background due to black holes forming and ringing down throughout the universe.

3.2.4 Double Neutron Star Coalescences

When two neutron stars collide, copious gravitational radiation is released during the final inspiralling orbits. The stochastic background of these gravitational wave bursts is among the most detectable of models considered here. While Regimbau and

de Freitas Pacheco[29] apply Monte Carlo techniques to determine the population stochastic background, we find that we can perform the calculation with numerical integration alone.

In the quadrupolar approximation, two masses, m_1 and m_2, which we will eventually take to be $1.4M_\odot$, that execute an inspiral will radiate according to:

$$\frac{\mathrm{d}E_{\mathrm{gw}}}{\mathrm{d}\nu} = \frac{(G\pi)^{2/3}}{3}\frac{m_1 m_2}{(m_1+m_2)^{1/3}}\nu^{-1/3}, \tag{3.27}$$

with a cutofff frequency equal to twice the Keplerian frequency at surface contact, or about 1500Hz.

The relationship between coalescence rate and the star formation rate is more complicated. The two massive stars of a double neutron star (DNS) progenitor system form according to the cosmic star formation rate. Being DNS system progenitors, they expend their nuclear fuel quickly (in a short 10^8 years) and manage to remain in bound orbits after the supernovae. The mass fraction of such systems is estimated to be $\lambda_{\mathrm{p}} = 1.85 \times 10^{-5} M_\odot^{-1}$ by simulation. Next, the newly formed neutron stars have some decreasing orbital separation and will eventually merge, but the merger timescale can vary widely. Further simulations show a minimum merger time of 2×10^5 years and a long-tailed merger probability density function of $P(\tau) = B/\tau$, where B is the normalization over the span 2×10^5 to 2×10^{10} years and has the value $B = 0.087$. Therefore, at each redshift z_{c}, the DNS merger rate is the integral over the DNS formation rate at each point in the past, $\mathrm{d}R_{\mathrm{f}}/\mathrm{d}z|_{z_{\mathrm{f}}}$, multiplied by the probability of merger at z_{c}, $P(\tau(z_{\mathrm{f}}, z_{\mathrm{c}})) \cdot \mathrm{d}t/\mathrm{d}z|_{z_{\mathrm{c}}}$:

$$\left.\frac{\mathrm{d}R_{\mathrm{c}}}{\mathrm{d}z}\right|_z = \int_z^5 P(\tau(z,z')) \left.\frac{\mathrm{d}t}{\mathrm{d}z}\right|_z \left.\frac{\mathrm{d}R_{\mathrm{SFR}}}{\mathrm{d}z}\right|_{z'} \mathrm{d}z'. \tag{3.28}$$

This tricky function can be numerically integrated at each z then substituted into our final expression:

$$\Omega_{\mathrm{gw}}(\nu_{\mathrm{o}}) = \frac{8\pi G}{3H_0^3 c^2}\nu_{\mathrm{o}} \int_{z_{\min}}^{z_{\max}(\nu_{\mathrm{o}})} \frac{1}{4\pi d_L^2(z)} \frac{\mathrm{d}R_{\mathrm{c}}}{\mathrm{d}z} \left.\frac{\mathrm{d}E_{\mathrm{gw}}}{\mathrm{d}\nu}\right|_{\nu=\nu_{\mathrm{o}}(1+z)} \mathrm{d}z. \tag{3.29}$$

Finally, we need limits of integration. On the lower end, we are constrained by duty cycle. As DNS coalescences are short-duration and rare events, one has to consider a very large volume before one can be continuously bathed in their gravitational waves. As the stochastic search is optimized for continuous stochastic backgrounds, we must constrain ourselves to search for sources at high duty-cycle redshifts. We define duty-cycle as following:

$$D(z) = \int_0^z \bar{\tau}(1+z') \left.\frac{\mathrm{d}R_\mathrm{c}}{\mathrm{d}z}\right|_{z'} \mathrm{d}z', \tag{3.30}$$

where $\bar{\tau}$ is the mean duration of the gravitational wave emission. It is multiplied by rate per unit redshift at each redshift to obtain an average number of events occurring simultaneously in the volume out to z. The redshift at which the duty-cycle is 1, a semi-arbitrary choice, is $z \approx 0.23$ for our star formation model. We exclude everything with lower duty cycle by setting $z_\mathrm{min} = 0.23$. At the upper end, we are constrained by the high-frequency radiation cutoff, so:

$$z_\mathrm{max} = \min\left\{\frac{1500\mathrm{Hz}}{\nu_\mathrm{o}} - 1, 5\right\}. \tag{3.31}$$

3.2.5 Neutron Star Bar Modes

Rapidly spinning neutron stars can become unstable to r-modes (rotational modes) of $l \geq 2$. The $l = 2$ mode deforms the neutron star to a bar-like geometry, and is often called a bar mode. Such geometry and kinematics give rise to copious gravitational radiation[31]. Unfortunately, there are several aspects of these models are controversial and perhaps over-optimistic, and as they affect the amplitude and spectral shape[25], we decline to search for this population.

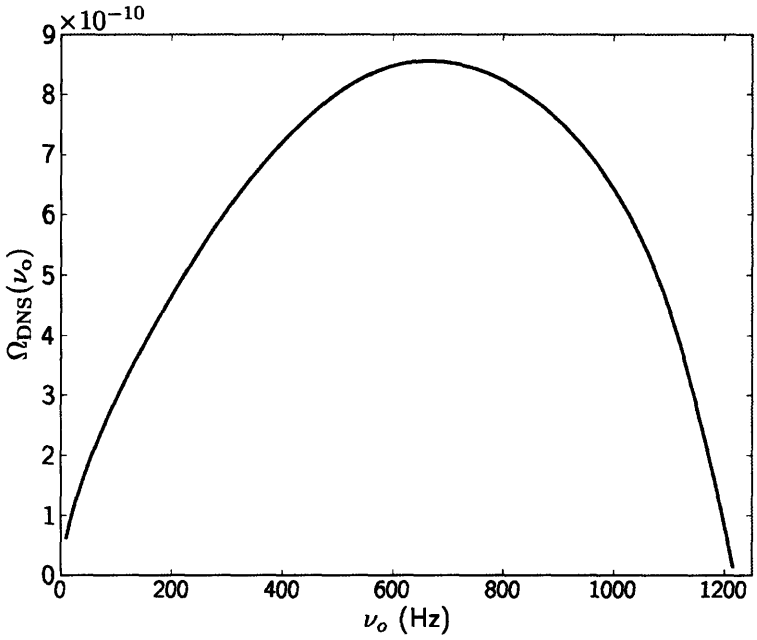

Figure 3-3: Expected stochastic gravitational wave background due to double neutron star mergers throughout the universe.

Chapter 4

A Search for Astrophysical Gravitational Radiation

With candidate spectra from chapter 3, and H1-H2 frequency vetoes from chapter 2, we are ready to design and execute a search. This chapter describes the design and validation of the search. Validation was performed on S4 and the first three months of S5 data, which I will call S5a. The data of S5a is described in section 5.1. All nine-digit times are GPS times, that is, seconds since the start of the GPS epoch, 00:00:00 UTC on January 6, 1980. Wherever two error bars follow a measurement, the first error bar is statistical uncertainty, and the second is systematic calibration uncertainty.

4.1 Search Pipeline

The search proceeds according to the standard stochastic search pipeline, largely described in chapter 1, with two additions – frequency vetoes and custom optimal filters. The code to produce and use optimal filters from spectra was recently written for use in the gravitational radiometer search [7] and works in the present context with only trivial modification. The code to produce frequency vetoes was written for the analysis of chapter 2. The analysis parameters, including PEM channels used are in Appendix A.

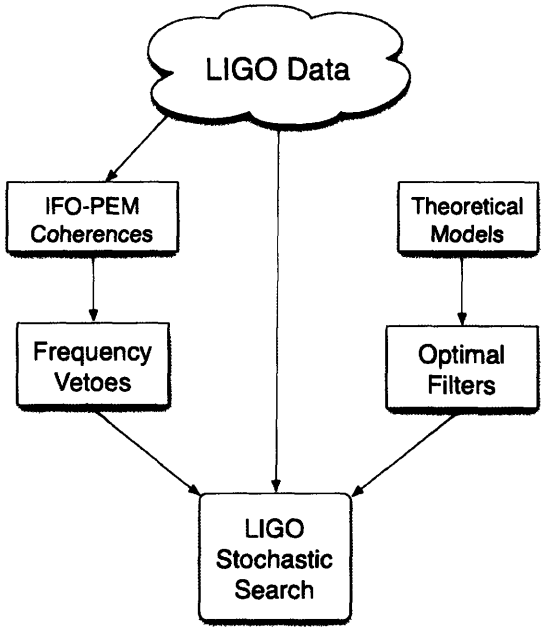

Figure 4-1: Flowchart of the pipeline used in this thesis to measure stochastic backgrounds of astrophysical gravitational waves. The LIGO stochastic analysis is described in references [9], [10], and [12].

4.2 Low-Frequency Validation with Hardware Injections

While we saw in chapter 2 that thresholding the coherence product maxima makes the resulting H1-H2 coherence appear clean, one way to gain confidence in the technique is to use it to successfully recover hardware injections. Hardware injections are gravitational wave-like differential strains induced by physically shaking optics at one end of each interferometer. For stochastic injections, the signals' spectral characteristics are generally designed to mimic a flat Ω_{gw} spectrum. We search for the injections in the sensitive region of detector response, 40-500Hz, where environmental correlations are also strongest. Successfully recovering the injected amplitude gives some confidence in the efficacy of a data analysis pipeline.

4.2.1 S4 Hardware Injections

Three S4 hardware injections were previously analyzed for H1-L1 and H2-L1, and are given in table 4.1 for comparison. The injection #1 is ignored due to missing calibration. During injection #4, H2's laser was unstable. Injection #5 was H1-H2 only. For each measured value, the first error bars are statistical uncertainties, and the second are the calibration uncertainties. Within a given injection segment, injected amplitudes are not the same for different pairs due to the inaccuracy of our knowledge of the calibration at the time that the injections were performed. V4 calibration was used. All analyzed injections were recovered by the standard stochastic analysis.

Injection	Start time	Duration	Injected $\Omega_{gw,0}$	Measured $\Omega_{gw,0}$
#2 (H1-L1)	794623800	3610	4.7×10^{-2}	$(4.1 \pm 0.1 \pm 0.4) \times 10^{-2}$
#2 (H2-L1)	794623800	3610	4.1×10^{-2}	$(3.6 \pm 0.2 \pm 0.3) \times 10^{-2}$
#3 (H1-L1)	794628333	1024	1.3×10^{-2}	$(1.3 \pm 0.2 \pm 0.1) \times 10^{-2}$
#3 (H2-L1)	794628333	1024	1.2×10^{-2}	$(0.8 \pm 0.3 \pm 0.1) \times 10^{-2}$
#4 (H1-L1)	794683400	20600	5.8×10^{-3}	$(4.9 \pm 0.2 \pm 0.5) \times 10^{-3}$

Table 4.1: S4 hardware injection results for H1-L1 and H2-L1 pairs. All injections were successfully recovered for both pairs. Start time is in GPS seconds and duration is in seconds.

Using our technique of generating frequency vetoes, we analyzed the relevant hardware injections in H1-H2. Results are given in table 4.2 with various thresholds. The threshold=1 case does not threshold the coherence product maxima at all, but still removes 60Hz harmonics and the pulsar injections, which occur at fixed frequencies and are present through much of the run.

All three S4 H1-H2 hardware injections were recovered, though the systematic calibration errors completely dominate the error. Calibration uncertainty is approximately 11%.

4.2.2 S5a Hardware Injections

During S5a, the beginning epoch of S5, two stochastic hardware injections were performed. For H1-L1 and H2-L1 standard stochastic searches, both injections were recovered, as summarized in table 4.3. Note that the table covers only triple coinci-

Injection/Threshold	Start time	Duration	Injected Ω_0	Measured Ω_0
#2 (H1-H2)	794623162	4498	4.43×10^{-2}	
threshold = 1.0	-	-		$(3.953 \pm .011 \pm .435) \times 10^{-2}$
threshold = 6.8×10^{-6}	-	-		$(3.948 \pm .014 \pm .434) \times 10^{-2}$
threshold = 3×10^{-7}	-	-		$(4.002 \pm .041 \pm .440) \times 10^{-2}$
#3 (H1-H2)	794628333	1024	1.03×10^{-2}	
threshold = 1.0	-	-		$(0.899 \pm .020 \pm .099) \times 10^{-2}$
threshold = 6.8×10^{-6}	-	-		$(0.896 \pm .025 \pm .099) \times 10^{-2}$
threshold = 3×10^{-7}	-	-		$(0.827 \pm .071 \pm .091) \times 10^{-2}$
#5 (H1-H2)	794623162	14398	5.42×10^{-3}	
threshold = 1.0	-	-		$(5.116 \pm .056 \pm .526) \times 10^{-3}$
threshold = 6.8×10^{-6}	-	-		$(5.260 \pm .074 \pm .579) \times 10^{-3}$
threshold = 3×10^{-7}	-	-		$(5.033 \pm .203 \pm .554) \times 10^{-3}$

Table 4.2: S4 hardware injection results for H1-H2. Thresholds are applied to the coherence product maxima to produce frequency vetoes, as described in chapter 2. Start time is in GPS seconds and duration is in seconds.

dence times for more direct comparison to the H1-H2 case. The H1-L1 and H2-L1 analyses were also successful over the full double coincidence intervals. Additionally, the set of PEM channels used is identical to the set used for S4 analysis, and the channels are listed in Appendix A. V2 calibration was used.

Injection	Start time	Duration	Nominal $\Omega_{gw,0}$	Measured $\Omega_{gw,0}$
#1 (H1-L1)	822198750	960	1	$0.92 \pm .04 \pm .10$
#1 (H2-L1)	822198750	960	1	$1.01 \pm .05 \pm .11$
#2 (H1-L1)	822201020	1152	10^{-2}	$(1.09 \pm .12 \pm .12) \times 10^{-2}$
#2 (H2-L1)	822201020	1152	10^{-2}	$(1.11 \pm .21 \pm .12) \times 10^{-2}$

Table 4.3: S5a hardware injection results for H1-L1 and H2-L1 pairs during triple coincidence times only. Both injections were successfully recovered for both pairs. Start time is in GPS seconds and duration is in seconds.

The same analysis was performed for H1-H2 in table 4.4 and all injections were recovered. As the threshold lowers, we do not see any systematic drift of the point estimate. We also see the lower bound of thresholding; for the weaker injection and lowest threshold, we fail to discriminate signal from noise.

Unfortunately, such high calibration uncertainties with such strong hardware injections do not constrain Ω_{instr}. Further studies with software injections at lower injection amplitudes are necessary to probe the effectiveness of this technique and

Injection	Start time	Duration	Nominal $\Omega_{gw,0}$	Measured $\Omega_{gw,0}$
#1 (H1-H2)	822198750	960	1	
Threshold = 1.00	-	-	$(964.63 \pm 2.56 \pm 106.11) \times 10^{-3}$	
Threshold = 4.02×10^{-6}	-	-	$(961.11 \pm 2.77 \pm 105.72) \times 10^{-3}$	
Threshold = 1.27×10^{-6}	-	-	$(958.65 \pm 2.98 \pm 105.45) \times 10^{-3}$	
Threshold = 4.02×10^{-7}	-	-	$(950.58 \pm 3.47 \pm 104.56) \times 10^{-3}$	
Threshold = 1.27×10^{-7}	-	-	$(935.84 \pm 4.64 \pm 102.94) \times 10^{-3}$	
Threshold = 4.02×10^{-8}	-	-	$(917.02 \pm 7.06 \pm 100.87) \times 10^{-3}$	
Threshold = 1.27×10^{-8}	-	-	$(86.49 \pm 1.29 \pm 9.29) \times 10^{-2}$	
Threshold = 4.02×10^{-9}	-	-	$(89.61 \pm 3.26 \pm 9.86) \times 10^{-2}$	
Threshold = 1.27×10^{-9}	-	-	$(9.48 \pm 1.22 \pm 1.04) \times 10^{-1}$	
#2 (H1-H2)	822201020	1152	10^{-2}	
Threshold = 1.00	-	-	$(961.74 \pm 9.65 \pm 105.79) \times 10^{-5}$	
Threshold = 4.02×10^{-6}	-	-	$(963.42 \pm 9.87 \pm 105.98) \times 10^{-5}$	
Threshold = 1.27×10^{-6}	-	-	$(96.86 \pm 1.04 \pm 10.65) \times 10^{-4}$	
Threshold = 4.02×10^{-7}	-	-	$(96.76 \pm 1.21 \pm 10.64) \times 10^{-4}$	
Threshold = 1.27×10^{-7}	-	-	$(96.82 \pm 1.62 \pm 10.65) \times 10^{-4}$	
Threshold = 4.02×10^{-8}	-	-	$(100.63 \pm 2.62 \pm 11.07) \times 10^{-4}$	
Threshold = 1.27×10^{-8}	-	-	$(97.41 \pm 6.23 \pm 10.72) \times 10^{-4}$	
Threshold = 4.02×10^{-9}	-	-	$(9.46 \pm 1.82 \pm 1.04) \times 10^{-3}$	
Threshold = 1.27×10^{-9}	-	-	$(9.78 \pm 4.44 \pm 1.08) \times 10^{-2}$	

Table 4.4: S5a hardware injection results for H1-H2 pairs during triple coincidence times. Thresholds are applied to the coherence product maxima to produce frequency vetoes, as described in chapter 2. We expect and assume an 11% systematic uncertainty, based on S4 calibrations. Start time is in GPS seconds and duration is in seconds.

determine a good threshold.

Chapter 5

S5a H1-H2 Results

The pipeline described in chapter 4 was run for H1-H2 on the S5a data set. We quote measured values of Ω_{gw} for a flat energy spectrum and astrophysical backgrounds of pulsars/magnetars, black hole ringdowns, and double neutron star coalescences. Unfortunately, the results here will stand only as a proof of concept. Before formal, Bayesian upper limits can be placed on physical quantities, we must bound Ω_{instr}, which remains a future work, and is described in the final section.

5.1 Data Selection

The analysis was performed over the S5a epoch, GPS times 815402926 to 823284014, Nov 07 2005 12:48:33 UTC to Feb 06 2006 18:00:00 UTC, or S5 start to the February commissioning break, while both H1 and H2 were in science mode and while there were no obvious problems with data quality. We omitted time intervals during which calibration is missing, when laser or electronics glitches appeared, when local wind speeds reached 30 miles per hour, and the 30 seconds prior to each loss of interferometer lock.

After restricting ourselves to double-coincidence times and making these data quality cuts, net live time was 7.1×10^6 seconds of the 7.8×10^6 in the epoch. The actual time run through the coherence portion of the pipeline and actual time run through the stochastic analysis will be smaller, since data can only be analyzed in

minimum length-chunks – 32 seconds for coherences and 578 seconds for the stochastic analysis.

5.2 S5a H1-H2 Coherence Spectrum

It is useful to examine properties of the coherence spectrum, as in chapter 2. Figure 5-1 shows us the H1-H2 coherence over the coherence product maxima approximation. Again, we see that the approximation follows the measured coherence quite closely above the $1/N$ line. Only near 60Hz harmonics, where non-linear interferometer effects occur, do we see noticeable deviation.

Post-veto coherence histograms can be seen in figure 5-2. They show that for all but the loosest thresholds, the excess coherence over null is very small. Note that this does not cover the high-coherence tail, where there are several discrete outliers. Coherence measurements indicate a clean coherence distribution for most thresholds.

5.3 Flat Ω_{gw} Spectrum

The flat Ω_{gw} is the standard target of the LIGO stochastic search. We present such a search with H1-H2 to directly compare sensitivity with H1-L1 in the band 40-500Hz. While the result cannot yet be construed as a physical statement, the error bar is sufficiently small that it may serve to whet the appetite for future H1-H2 work. Again, calibration uncertainty is assumed to be 11%, based on S4 calibration.

5.3.1 Result

In table 5.1, we immediately see that for certain thresholds, the point estimate raised to significantly non-zero values. This is clear indication that negative Ω_{instr} had been removed. The subsequent lowering indicates that positive correlation was removed also. Unfortunately, we don't know if all instrumental correlation is removed in the end, despite a null result. The error bar increases with decreasing threshold because we are analyzing less and less data.

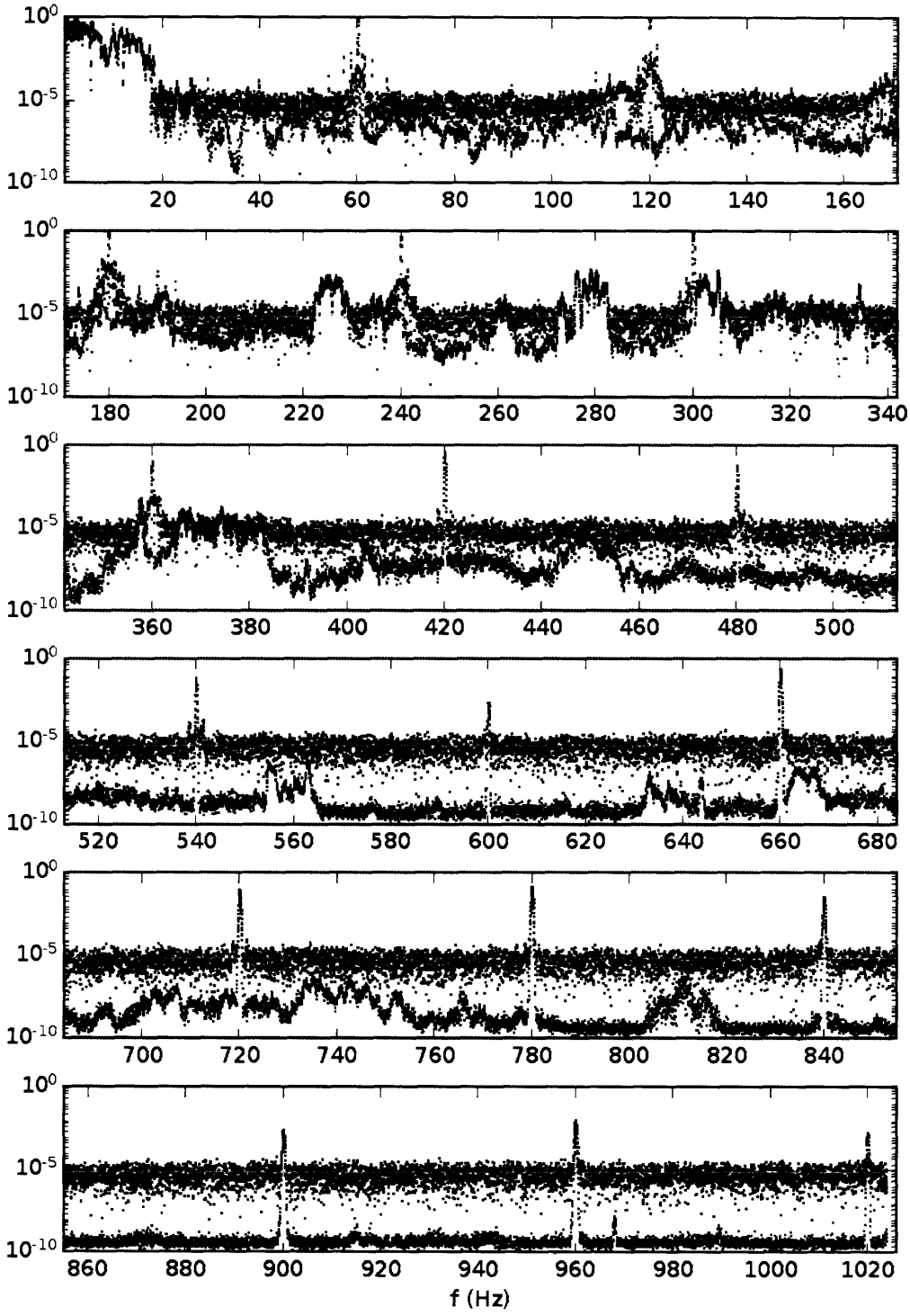

Figure 5-1: S5a H1-H2 coherence and the IFO-PEM coherence product maxima approximation. The top trace is the direct H1-H2 coherence and the lower trace represents the coherence product maxima. The gray, horizontal line at $1/N \approx 10^{-5}$ is the noise floor of the former.

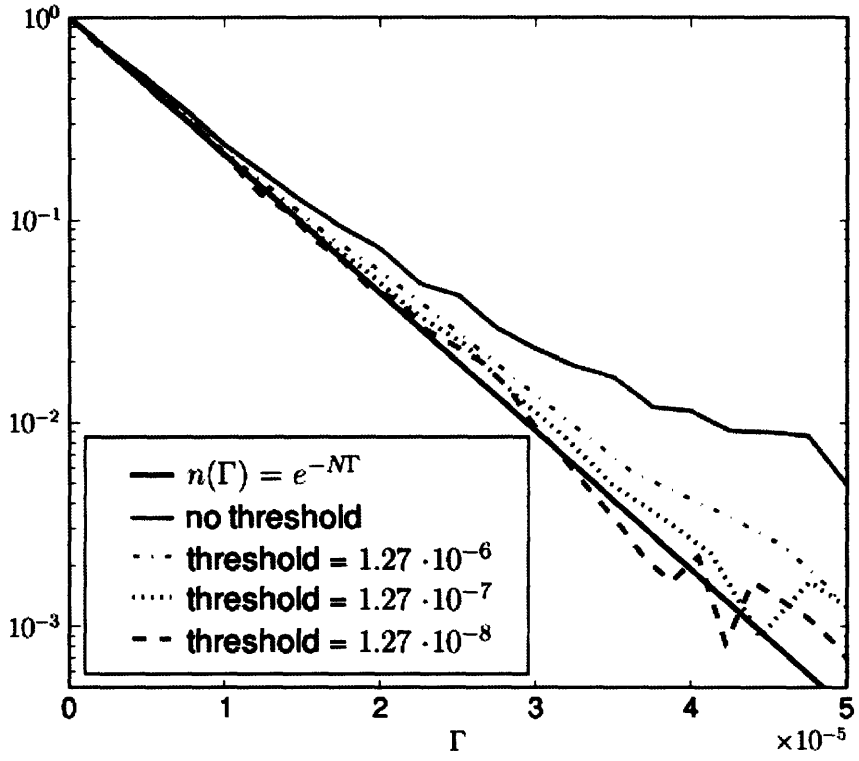

Figure 5-2: Normalized coherence histograms for surviving S5a H1-H2 coherence after veto.

We have no *a priori* method of choosing a threshold, but it would seem that everything below a threshold of 4.02×10^{-8} yields a non-detection. We will use this threshold as a test case for our diagnostics. The error bar of 4.22×10^{-6} is an estimated factor of ~ 4 better than the corresponding H1-L1 error for the same analysis. Marginalizing over Ω_{instr} will surely erode this advantage, but this result is encouraging nonetheless. In particular, our error bar is well under the BBN limit (see section 1.3.4). The full S5 data set should be at least four times as long as the S5a data set, halving the error bar in the final analysis. If the marginalization does not inflate the error bar by more than a factor of eight, then LIGO will be ready to make a meaningful physical statement at the end of S5.

Threshold	Measured Point Estimate	SNR	In-band BW	Sensitive BW
1.00×10^{0}	$(6.14 \pm 1.54 \pm .68) \times 10^{-6}$	3.6	.912	.939
4.02×10^{-6}	$(2.94 \pm 1.57 \pm .32) \times 10^{-6}$	1.8	.763	.919
1.27×10^{-6}	$(4.52 \pm 1.65 \pm .50) \times 10^{-6}$	2.6	.666	.848
4.02×10^{-7}	$(11.46 \pm 1.94 \pm 1.26) \times 10^{-6}$	5.0	.531	.667
1.27×10^{-7}	$(17.19 \pm 2.57 \pm 1.89) \times 10^{-6}$	5.4	.364	.415
4.02×10^{-8}	$(7.25 \pm 4.22 \pm .80) \times 10^{-6}$	1.7	.220	.177
1.27×10^{-8}	$(15.62 \pm 10.30 \pm 1.72) \times 10^{-6}$	1.5	.102	.036
4.02×10^{-9}	$(2.13 \pm 2.90 \pm .23) \times 10^{-5}$	0.7	.026	.007
1.27×10^{-9}	$(15.22 \pm 12.18 \pm 1.67) \times 10^{-4}$	1.2	.005	.000

Table 5.1: S5a H1-H2 Flat Spectrum Results. Error bars represent statistical uncertainty, then calibration uncertainty. SNR is calculated using the root sum squares of the uncertainties. The final two columns hold the fraction of bandwidth remaining after veto. In-band BW refers to the entire analysis band of 40-500Hz. Sensitive BW refers to the frequency region between the 1st and 99th percentiles of cumulative sensitivity (as integrated over frequency), or 77.25-160.84375Hz. Calibration uncertainty is assumed to be 11%.

5.3.2 Diagnostic Checks

Here we review diagnostic plots for a threshold of 4.02×10^{-8}, figures 5-3 through 5-5. They are unfortunately inconclusive as to residual correlation in the result.

Figure 5-3 shows the cumulative point estimate as additional data is included over the course of the run. In the absence of systematic correlations between instruments, the point estimate error bars would continuously constrict around zero. This behavior we see in this plot seems perfectly consistent with a null result.

Figure 5-4 shows the coherence and the coherence product maxima again, but this time, we show the vetoed regions in red. Figure 5-5 shows us the relative contribution of each surviving frequency bin. We see that there are clear high coherence outliers, probably from non-linear up-conversion of seismic or acoustic disturbances, optical effects, or other, unmonitored influences which should be investigated further. In future analyses, these can certainly be thresholded and removed, since we believe that a stochastic background will be relatively smooth and will not contain sharp peaks.

One common diagnostic is the Fourier Transform of the point estimate's frequency-domain integrand, in which one obtains the point estimate as a function of time-shift.

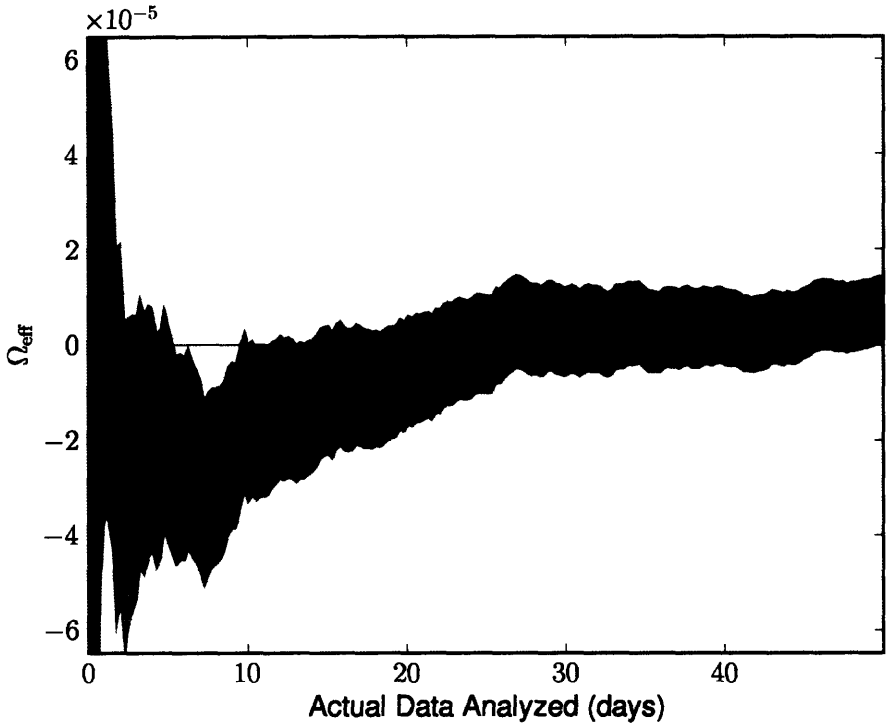

Figure 5-3: The running point estimate of the S5a H1-H2 flat $\Omega_{\rm gw}$ stochastic analysis. At each time, the ordinate is the point estimate as integrated over all prior data. The blue region is the 90% confidence region, i.e., 1.65σ. The data shown have been smoothed via interpolation.

That is, the value at a given time-shift is the point estimate that would have been measured with that time-shift introduced between the data channels, integrated over the data set. However, with this analysis, we have cut out frequency bins wholesale, and the effect of such notching is to make the time-domain ring. It seems likely that this diagnostic is no longer useful with the addition of frequency vetoes.

In summary, we see no indication of environmental contamination still present in the H1-H2 stochastic result with an applied threshold of 4.02×10^{-8}. Unfortunately, our diagnostics do not discount the possibility. Again, what remains is to quantify that residual contamination.

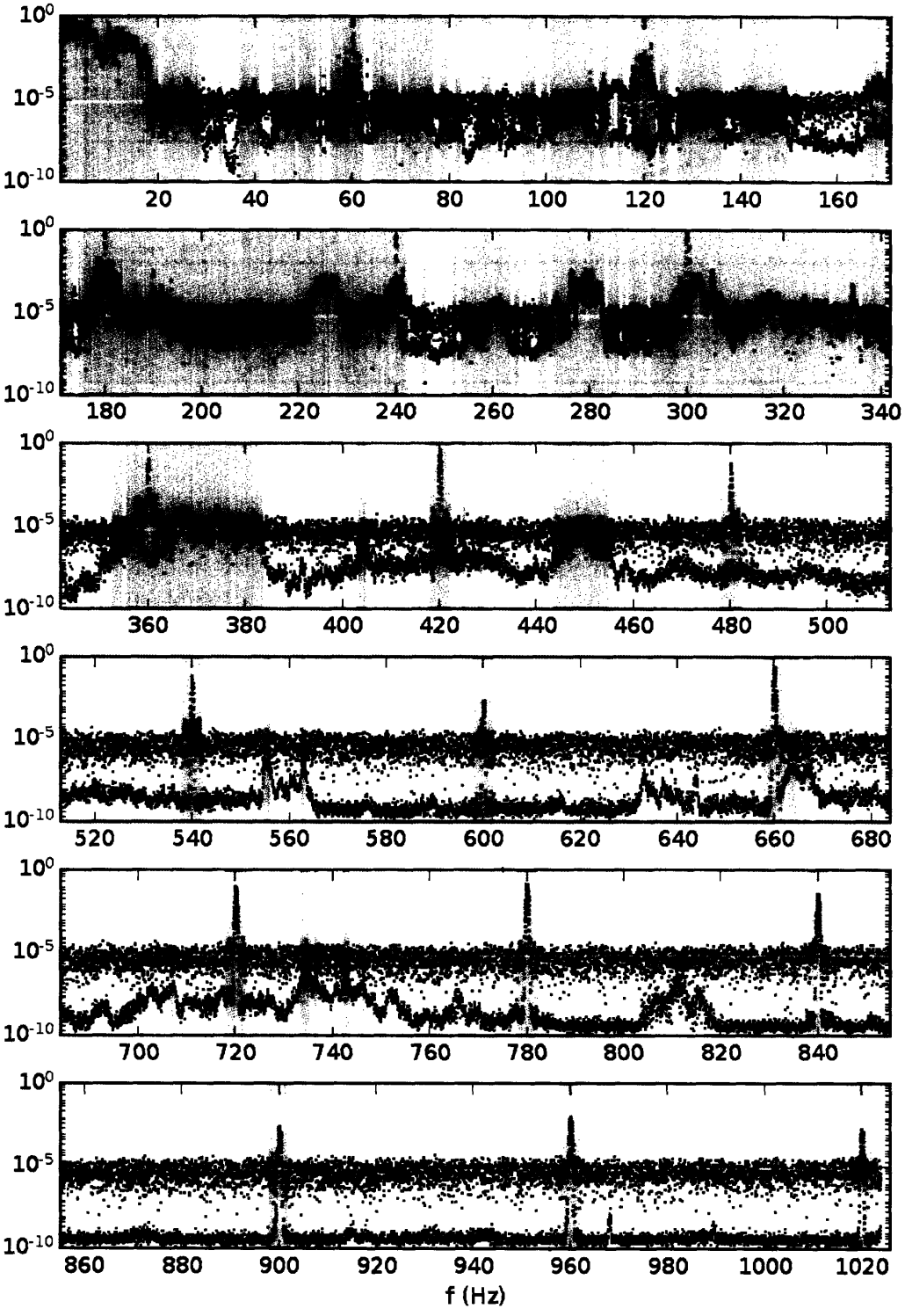

Figure 5-4: S5a H1-H2 coherence and the IFO-PEM coherence product maxima approximation, with threshold= 4.02×10^{-8} vetoed regions highlighted in red. The top trace is the direct H1-H2 coherence and the lower trace represents the coherence product maxima. The gray, horizontal line at $1/N \approx 10^{-5}$ is the noise floor of the former.

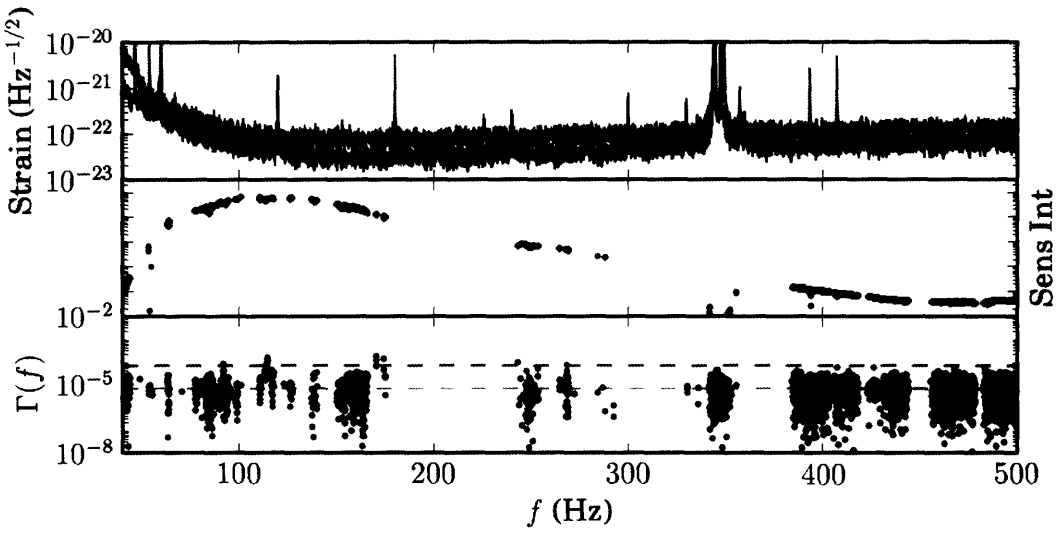

Figure 5-5: Top: H1 and H2 interferometer strain noise curves as measured in January 2006, about midway through S5a. Middle: H1-H2 stochastic search sensitivity integrand, with vetoes applied. Frequencies with larger sensitivity integrands contribute more to the point estimate. Units are not particularly meaningful, so we omit them. The scaling on the y axis is logarithmic. Integrating from low frequency to high, 1% and 99% accumulated sensitivity percentiles are 77.25Hz and 160.84375Hz, respectively. Bottom: Coherence from frequency bins which survive the frequency veto with threshold 4.02×10^{-8}. The grey, dashed line indicates $1/N$, the coherence noise floor, and the red, dashed line indicates $10.4/N$, the coherence level below which one would expect all coherences, were the coherence all drawn from an uncorrelated distribution ($\exp(-N\Gamma)$), with a false rate of approximately 1 in 32768.

5.4 Pulsar/Magnetar Results

For a background of unresolved pulsars, we expected to see nothing and our expectations have been met in table 5.2. We are six orders of magnitude away from being able to detect the pulsar background as predicted. The magnetar background may be as much as a factor of two stronger overall, but again produce the same spectral shape. With both models having large uncertainties in amplitude, we are perhaps five orders of magnitude in sensitivity from any constraining statement on these populations.

A brief note on orders of magnitude in point estimates: The flat search returned very small values because the signal for which we optimally filter has (constant) magnitude 1, and our sensitivity is well below that. Here, the signal for which we are optimally filtering has very small input amplitude and our sensitivity is well above

that, so we see very large point estimates.

Threshold	Measured Point Estimate	SNR
Threshold $= 1.00 \times 10^{0}$	$(22.19 \pm 1.23 \pm 2.44) \times 10^{6}$	8.1
Threshold $= 4.02 \times 10^{-6}$	$(1.85 \pm 1.36 \pm .20) \times 10^{6}$	1.3
Threshold $= 1.27 \times 10^{-6}$	$(2.90 \pm 1.47 \pm .32) \times 10^{6}$	1.9
Threshold $= 4.02 \times 10^{-7}$	$(1.71 \pm 1.66 \pm .19) \times 10^{6}$	1.0
Threshold $= 1.27 \times 10^{-7}$	$(2.27 \pm 2.03 \pm .25) \times 10^{6}$	1.1
Threshold $= 4.02 \times 10^{-8}$	$(1.23 \pm 2.60 \pm .14) \times 10^{6}$	0.5
Threshold $= 1.27 \times 10^{-8}$	$(4.82 \pm 3.92 \pm .53) \times 10^{6}$	1.2
Threshold $= 4.02 \times 10^{-9}$	$(2.22 \pm 1.02 \pm .24) \times 10^{7}$	2.1
Threshold $= 1.27 \times 10^{-9}$	$(6.30 \pm 3.25 \pm .73) \times 10^{7}$	2.0

Table 5.2: S5a H1-H2 Pulsar/Magnetar Results

5.5 Black Hole Ringdown Results

In table 5.3, we see no indication of a black hole ringdown background. Our sensitivity is six orders of magnitude away from detection at the estimated strength. Constraining physical statements might occur at five orders of magnitude sensitivity improvement.

Threshold	Measured Point Estimate	SNR
Threshold $= 1.00 \times 10^{0}$	$(35.54 \pm 1.73 \pm 3.91) \times 10^{5}$	8.3
Threshold $= 4.02 \times 10^{-6}$	$(4.70 \pm 1.99 \pm .52) \times 10^{5}$	2.3
Threshold $= 1.27 \times 10^{-6}$	$(6.87 \pm 2.17 \pm .76) \times 10^{5}$	3.0
Threshold $= 4.02 \times 10^{-7}$	$(7.45 \pm 2.47 \pm .82) \times 10^{5}$	2.9
Threshold $= 1.27 \times 10^{-7}$	$(1.84 \pm 3.04 \pm .20) \times 10^{5}$	0.6
Threshold $= 4.02 \times 10^{-8}$	$(0.27 \pm 4.01 \pm .03) \times 10^{5}$	0.1
Threshold $= 1.27 \times 10^{-8}$	$(6.26 \pm 5.93 \pm .69) \times 10^{5}$	1.0
Threshold $= 4.02 \times 10^{-9}$	$(3.06 \pm 1.39 \pm .34) \times 10^{6}$	2.1
Threshold $= 1.27 \times 10^{-9}$	$(7.72 \pm 4.25 \pm .85) \times 10^{6}$	1.8

Table 5.3: S5a H1-H2 Blackhole Ringdown Results

5.6 Double Neutron Star Coalescence Results

The most detectable of our astrophysical spectra, a background of neutron star-neutron star coalescences is again a null result, as seen in figure 5.4. Unfortunately, we

are now three or four orders of magnitude from a physically interesting result, though that may be within the range of Advanced LIGO's H1-H2. It seems that astrophysical stochastic backgrounds are beyond the reach of first generation gravitational wave detectors and at the very edges of the second.

Threshold	Measured Point Estimate	SNR
Threshold $= 1.00 \times 10^{0}$	$(27.81 \pm 4.66 \pm 3.06) \times 10^{3}$	5.0
Threshold $= 4.02 \times 10^{-6}$	$(7.20 \pm 4.76 \pm .80) \times 10^{3}$	1.5
Threshold $= 1.27 \times 10^{-6}$	$(10.55 \pm 5.05 \pm 1.16) \times 10^{3}$	2.0
Threshold $= 4.02 \times 10^{-7}$	$(29.60 \pm 5.93 \pm 3.26) \times 10^{3}$	4.4
Threshold $= 1.27 \times 10^{-7}$	$(48.81 \pm 7.89 \pm 5.37) \times 10^{3}$	5.1
Threshold $= 4.02 \times 10^{-8}$	$(2.03 \pm 1.27 \pm .22) \times 10^{4}$	1.6
Threshold $= 1.27 \times 10^{-8}$	$(3.43 \pm 3.19 \pm .38) \times 10^{4}$	1.1
Threshold $= 4.02 \times 10^{-9}$	$(7.63 \pm 11.35 \pm .84) \times 10^{4}$	0.7
Threshold $= 1.27 \times 10^{-9}$	$(2.65 \pm 1.80 \pm .29) \times 10^{6}$	1.5

Table 5.4: S5a H1-H2 Double Neutron Star Coalescence Results

5.7 Future Prospects

This thesis has demonstrated that through IFO-PEM coherences, we can derive vetoes that significantly reduce environmental contributions to H1-H2 coherence. However, we simply do not know how much environmental contribution remains. The most important work to be done is to quantitatively bound Ω_{instr} so that we can translate an estimate of Ω_{eff} into an estimate of Ω_{gw}. This translation is done by Bayesian marginalization, similar to how we account for calibration uncertainty in H1-L1 and H2-L1 upper limits[12]. Thus, with a bound on Ω_{instr}, H1-H2 results have equal standing to H1-L1 and H2-L1 stochastic results. Allen and Romano [5] considered this briefly, so some of the formalism is in place.

If we cannot bound Ω_{instr} analytically, then we can never prove that we have identified all persistent, broadband, common, local noise. Nonetheless, our empirical diagnostics might still grant us some confidence in H1-H2's efficacy as a working detector pair, just as we have gained confidence in H1-L1. For every upper limit set by H1-L1 and H2-L1, a corroboration of non-detection by H1-H2 adds confidence. When

the day comes that H1-L1 and H2-L1 register a detection, the added corroboration of H1-H2 will provide tremendously greater confidence, formal proof or not.

Astrophysical populations of gravitational wave emitters seem firmly outside the range of LIGO, and may be detected by Advanced LIGO under optimistic parameter estimations. This thesis has demonstrated that the kilohertz region is largely free from environmental correlations and that the way is clear to make stochastic background observations of astrophysical interest.

The LIGO Scientific Collaboration hopes to use H1-H2 to improve the stochastic upper limit for the S5 data set now being collected; to what extent and in what capacity will depend on how well we can bound Ω_{instr}.

Appendix A

Analysis parameters

Table A.1 contains the parameters used for the stochastic searches of this thesis. They are the same for S4 and S5a except where explicitly called out.

In tables A.2-A.4, we list all PEM channels used to generate the coherence product maxima and subsequent frequency vetoes. Those channels recorded at high sampling rates (actually, only `H0:PEM-LVEA_MIC` and the `LSC-DARM_ERR` channels) were low-pass filtered and down-sampled for analysis. The low-pass filtering was accomplished with an 8th order Chebyshev Type 1 filter. Filtering was applied forwards, then backwards in order to achieve zero phase delay.

Parameter	Value
Frequency Range	[40,500]Hz
Frequency Resolution	1/32Hz
Resample Rate	1024Hz
Transient Buffer	1s
Data channel	LSC-DARM_ERR
Windowing Function	Hann
Window Duration	192s
Window Overlap	50%
High-pass Filter 3dB Freq	30Hz
High-pass Filter Order	6
Calibration Version (S4)	V4 (final)
Calibration Version (S5)	V2

Table A.1: Analysis parameters used in the stochastic searches of this thesis.

Channel name	Original Sampling Rate	Resampled Rate
H0:PEM-LVEA_SEISX	256	256
H0:PEM-LVEA_SEISY	256	256
H0:PEM-LVEA_SEISZ	256	256
H0:PEM-MX_SEISX	256	256
H0:PEM-MX_SEISY	256	256
H0:PEM-MX_SEISZ	256	256
H0:PEM-MY_SEISX	256	256
H0:PEM-MY_SEISY	256	256
H0:PEM-MY_SEISZ	256	256
H0:PEM-EX_SEISX	256	256
H0:PEM-EX_SEISY	256	256
H0:PEM-EX_SEISZ	256	256
H0:PEM-EY_SEISX	256	256
H0:PEM-EY_SEISY	256	256
H0:PEM-EY_SEISZ	256	256
H0:PEM-PSL1_ACCX	2048	2048
H0:PEM-PSL1_ACCZ	2048	2048
H0:PEM-PSL2_ACCX	2048	2048
H0:PEM-PSL2_ACCZ	2048	2048
H0:PEM-BSC1_ACCY	2048	2048
H0:PEM-BSC2_ACCX	2048	2048
H0:PEM-BSC2_ACCY	2048	2048
H0:PEM-BSC3_ACCX	2048	2048
H0:PEM-BSC4_ACCX	2048	2048
H0:PEM-BSC4_ACCY	2048	2048
H0:PEM-BSC5_ACCX	2048	2048
H0:PEM-BSC6_ACCY	2048	2048
H0:PEM-BSC7_ACCX	2048	2048
H0:PEM-BSC8_ACCY	2048	2048
H0:PEM-BSC9_ACC1X	2048	2048
H0:PEM-BSC10_ACC1Y	2048	2048
H0:PEM-HAM1_ACCX	2048	2048
H0:PEM-HAM1_ACCZ	2048	2048
H0:PEM-HAM3_ACCX	2048	2048
H0:PEM-HAM7_ACCX	2048	2048
H0:PEM-HAM7_ACCZ	2048	2048
H0:PEM-HAM9_ACCX	2048	2048
H0:PEM-ISCT1_ACCX	2048	2048
H0:PEM-ISCT1_ACCY	2048	2048
H0:PEM-ISCT1_ACCZ	2048	2048
H0:PEM-ISCT4_ACCX	2048	2048
H0:PEM-ISCT4_ACCY	2048	2048
H0:PEM-ISCT4_ACCZ	2048	2048

Table A.2: PEM channels used to generate vetoes, original sampled rates, and the downsampled rate used.

Channel name	Original Sampling Rate	Resampled Rate
H0:PEM-ISCT7_ACCX	2048	2048
H0:PEM-ISCT7_ACCY	2048	2048
H0:PEM-ISCT7_ACCZ	2048	2048
H0:PEM-ISCT10_ACCX	2048	2048
H0:PEM-ISCT10_ACCY	2048	2048
H0:PEM-ISCT10_ACCZ	2048	2048
H0:PEM-LVEA_MIC	16384	2048
H0:PEM-PSL1_MIC	2048	2048
H0:PEM-PSL2_MIC	2048	2048
H0:PEM-BSC5_MIC	2048	2048
H0:PEM-BSC6_MIC	2048	2048
H0:PEM-BSC7_MIC	2048	2048
H0:PEM-BSC8_MIC	2048	2048
H0:PEM-BSC9_MIC	2048	2048
H0:PEM-BSC10_MIC	2048	2048
H0:PEM-IOT1_MIC	2048	2048
H0:PEM-IOT7_MIC	2048	2048
H0:PEM-ISCT1_MIC	2048	2048
H0:PEM-ISCT4_MIC	2048	2048
H0:PEM-ISCT7_MIC	2048	2048
H0:PEM-ISCT10_MIC	2048	2048
H0:PEM-LVEA_MAGX	2048	2048
H0:PEM-LVEA_MAGY	2048	2048
H0:PEM-LVEA_MAGZ	2048	2048
H0:PEM-BSC1_MAG1X	2048	2048
H0:PEM-BSC1_MAG1Y	2048	2048
H0:PEM-BSC1_MAG1Z	2048	2048
H0:PEM-BSC5_MAGX	2048	2048
H0:PEM-BSC5_MAGY	2048	2048
H0:PEM-BSC5_MAGZ	2048	2048
H0:PEM-BSC6_MAGX	2048	2048
H0:PEM-BSC6_MAGY	2048	2048
H0:PEM-BSC6_MAGZ	2048	2048
H0:PEM-BSC9_MAGX	2048	2048
H0:PEM-BSC9_MAGY	2048	2048
H0:PEM-BSC9_MAGZ	2048	2048
H0:PEM-BSC10_MAGX	2048	2048
H0:PEM-BSC10_MAGY	2048	2048
H0:PEM-BSC10_MAGZ	2048	2048
H0:PEM-COIL_MAGX	2048	2048
H0:PEM-COIL_MAGZ	2048	2048
H0:PEM-RADIO_LVEA	2048	2048
H0:PEM-RADIO_CS_1	2048	2048

Table A.3: PEM channels used to generate vetoes, original sampled rates, and the downsampled rate used (continued).

Channel name	Original Sampling Rate	Resampled Rate
H0:PEM-RADIO_CS_2	2048	2048
H0:PEM-LVEA2_V1	2048	2048
H0:PEM-LVEA2_V2	2048	2048
H0:PEM-LVEA2_V3	2048	2048
H0:PEM-MX_V1	2048	2048
H0:PEM-MX_V2	2048	2048
H0:PEM-MY_V1	2048	2048
H0:PEM-MY_V2	2048	2048
H0:PEM-EX_V1	2048	2048
H0:PEM-EX_V2	2048	2048
H0:PEM-EY_V1	2048	2048
H0:PEM-EY_V2	2048	2048

Table A.4: PEM channels used to generate vetoes, original sampled rates, and the downsampled rate used (continued).

Bibliography

[1]

[2] LIGO laboratory home page for interferometer sensitivities. URL: `http://www.ligo.caltech.edu/~lazz/distribution/LSC_Data/`.

[3] Lazzarini A and Weiss R. LIGO science requirements document, 1996. LIGO DCC Number LIGO-E950018-02-E.

[4] Penzias A and Wilson R. A measurement of excess antenna temperature at 4080 mc/s. *Astrophysical Journal*, 142:419–421, 1965.

[5] Bruce Allen and Joseph Romano. Detecting a stochastic background of gravitational radiation: Signal processing strategies and sensitivities. *Phys. Rev. D*, 59(102001), October 1997. gr-qc/9710117.

[6] Allen B., Hua W., and Ottewill A. Automatic cross-talk removal from multi-channel data, 1999. gr-qc/9909083.

[7] Stefan Ballmer. *LIGO Interferometer Operating at Design Sensitivity with Application to Gravitational Radiometer.* PhD thesis, Massachusetts Institute of Technology, May 2006.

[8] Misner C, Thorne K, and Wheeler J. *Gravitation.* W. H. Freeman and Company, 1973.

[9] Abbott B et al. Searching for a stochastic background of gravitational waves with LIGO. Unpublished manuscript; astro-ph/0608606.

[10] Abbott B et al. Analysis of first LIGO science data for stochastic gravitational waves. *Phys. Rev. D*, 69(122004), 2004. gr-qc/0312088.

[11] Abbott B. et al. Detector description and performance for the first coincidence observations between LIGO and GEO. *Nuclear Instruments and Methods in Physics Research A*, 517:154–179, 2004.

[12] Abbott B et al. Upper limits on a stochastic background of gravitational waves. *Phys. Rev. Lett.*, 95(221101), 2005. astro-ph/0507254.

[13] Cyburt R. et al. New BBN limits on physics beyond the standard model from 4He. *Astroparticle Physics*, 23:313–323, April 2005. astro-ph/0408033.

[14] Dietz A et al. Calibration of the ligo detectors for s4, 2005. LIGO DCC Number LIGO-T050262-00-D.

[15] Henning Vahlbruch et al. Coherent control of vacuum squeezing in the gravitational-wave detection band. *Phys. Rev. Lett.*, 97(011101), 2006.

[16] Uchiyama T et al. Cryogenic cooling of a sapphire mirror-suspension for interferometric gravitational wave detectors. *Physics Letters A*, 242(4):211–214, 1998.

[17] Gabriela González. Suspensions thermal noise in the LIGO gravitational wave detector. *Classical and Quantum Gravity*, 17(4409), 2000.

[18] David Hogg. Distance measures in cosmology, 1999. Published only to the arXiv.org e-print database. astro-ph/9905116.

[19] Sylvestre J and Tinto M. Noise characterization for LISA. *Phys. Rev. D*, 68(102002), 2003.

[20] Maggiore M. Gravitational wave experiments and early universe cosmology. *Physics Reports*, 331:283–367, 2000.

[21] Orestis Malaspinas and Riccardo Sturani. Detecting a stochastic background of gravitational waves by correlating n detectors. *Class. Quantum Grav.*, 23:319–327, 2006.

[22] Vuk Mandic and Alessandra Buonanno. Accessibility of the pre-big-bang models to LIGO, 2005. astro-ph/0510341.

[23] Christensen N. Measuring the stochastic gravitational-radiation background with laser-interferometric antennas. *Phys. Rev. D*, 46(5250), 1992.

[24] Cristiano Porciani and Piero Madau. On the association of gamma-ray bursts with massive stars: Implications for number counts and lensing statistics. *The Astrophysical Journal*, 548:522–531, 2001.

[25] Tania Regimbau. The astrophysical background, 2005. Virgo Note VIR-NOT-OCA1390-307.

[26] Peter R. Saulson. Thermal noise in mechanical experiments. *Phys. Rev. D*, 42(8), 1990.

[27] Regimbau T. and de Freitas Pacheco. Cosmic background of gravitational waves from rotating neutron stars. *Astronomy and Astrophysics*, 376:381–385, 2001.

[28] Regimbau T. and de Freitas Pacheco. Gravitational wave background from magnetars. *Astronomy and Astrophysics*, 447:1–7, 2006.

[29] Regimbau T. and de Freitas Pacheco. Stochastic background from coalescences of NS-NS binaries. *The Astrophysical Journal*, 2006. In press.

[30] Ferrari V., Matarrese S., and Schneider R. Gravitational wave background from a cosmological population of core-collapse supernovae. *Monthly Notices of the Royal Astronomical Society*, 303:247–257, 1999.

[31] Ferrari V., Matarrese S., and Schneider R. Stochastic background of gravitational waves generated by a cosmological population of young, rapidly rotating neutron stars. *Monthly Notices of the Royal Astronomical Society*, 303:258, 1999.